Amplitude vacillation in baroclinic flows

Amplitude Vacillation in Baroclinic Flows
Chapter 3 in T. von Larcher and P. Williams: *Modeling Atmospheric and Oceanic Flows: Insights from Laboratory Experiments and Numerical Simulations.*

Wolf-Gerrit Früh

School of Engineering and Physical Sciences, Heriot-Watt University, Edinburgh EH14 4AS, UK

Abstract

This chapter will introduce the phenomenology of vacillation in baroclinic flows based on experimental data, CFD and low-order numerical models. The processes leading to vacillation of a steady baroclinic wave will be discussed in terms of nonlinear interactions between different wave modes and between waves and the azimuthally or longitudinally averaged baroclinic flow. Complementing the review of the literature on amplitude vacillation, some new material will be presented to discuss the effect of the presence of lateral boundary layers in laboratory experiments and of the Prandtl number on feedback between the vacillating waves and the Ekman transport in the boundary layers. In the later sections, other forms of vacillation will be discussed and, finally, the role of vacillation in the transition to chaos and turbulence will be briefly addressed.

1. Phenomenology of Amplitude Vacillation

The first reference to the term 'vacillation' in reference to baroclinic flows, with a qualitative description, can be found in a brief note from January 1953 by *Hide* [28] on observations in a rotating baroclinic annulus: '*One cycle of this phenomenon, which has been termed 'vacillation' begins (say) with a symmetrical wave pattern with its continuous 'jet'. Some seconds later there is a distinct leaning backward of the troughs and a decrease of their width. This is followed by the troughs returning to N.-S. orientation and then leaning forward in preparation of the stage when the 'jet' stream is actually interrupted and intense cyclones are formed in the position of the wave troughs. The cyclones decay and the 'jet' is re-established; the wave pattern returns to the initial stage and the cycle starts again. The period corresponds to a few 'weeks'.*'. A full description of his observations can be found in *Hide* [29] and two typical snapshots of a vacillating wave 3 are shown in Figure 1. While it will become apparent in this chapter that this excerpt describes structural vacillation, rather than amplitude vacillation, it initiated detailed research into vacillating flows in many places.

Email address: w.g.fruh@hw.ac.uk, (Wolf-Gerrit Früh)

Preprint submitted to Wiley, 2014, ISBN 978-1-118-85593-5 *September 11, 2014*

This term 'vacillation' was subsequently taken up as a technical term and its definition refined, distinguishing between amplitude vacillation and shape vacillation [32]. *Fowlis and Pfeffer* [15] characterised amplitude vacillation based on an array of thermistors in a large baroclinic annulus. Since then, amplitude vacillation has been investigated in laboratory experiments with a range of thermally-driven baroclinic rotating annulus experiments, for example by *White and Koschmieder* [86], *Tamaki and Ukaji* [78], and *Sitte and Egbers* [74] in addition to those by Raymond Hide and Richard Pfeffer. While these experiments generated the baroclinic flow by thermal forcing of the side-walls, it can also be mechanically forced by a differentially rotating lid in contact with the upper layer of a two-layer fluid. This system has also been investigated in detail by *Hart* [22] and successors. Like the thermally driven annulus, this two-layer experiment has also shown amplitude vacillation both, in experiments with two immiscible fluids [23, 24] and with salt-stratified water [14].

Another example of flow observations referred to as amplitude vacillation is from a thermally driven annulus which is rotated so rapidly that the centrifugal term outweighs terrestrial gravity [2, 56, 73]. In that case, the fluid is no longer stably stratified and the resulting flow is closer to rotationally constrained Rayleigh-Bénard convection than to baroclinic instability. The term vacillation is also used to describe atmospheric phenomena, such as tropospheric wave-zonal flow fluctuations [40, 12], the stratospheric vacillation [10, 67, 77], or sea-surface temperature (SST) fluctuations [82], and for climate fluctuations [76].

A widely accepted definition of amplitude vacillation (AV) is now that it is a (fairly) regular oscillation of the magnitude of a well-defined wave mode while the spatial structure remains (essentially) unchanged. A more complex form of vacillation is modulated amplitude vacillation (MAV) [71, 17] which frequently displays chaotic oscillations and usually involves fluctuations of several wave modes of different spatial structure. A periodic amplitude vacillation of a wave number 2 and a chaotic modulated amplitude vacillation are illustrated in Figure 2, both taken from the Direct Numerical Simulations of an air-filled annulus described by *Randriamampianina et al.* [69] and *Randriamampianina and Crespo Del Arco* [68] in this book. A special case of a flow which appears like a modulated amplitude vacillation is the superposition of two steady wave modes; this has been termed interference vacillation [55, 44].

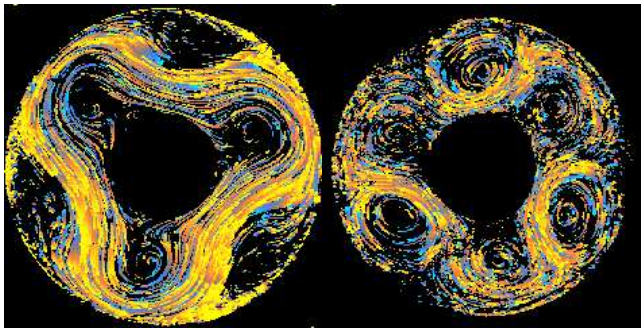

Figure 1: Illustration of two flow stages within an amplitude vacillation cycle (Peter Read, published in [41], ©John Wiley & Sons, used with permission).

a) b)

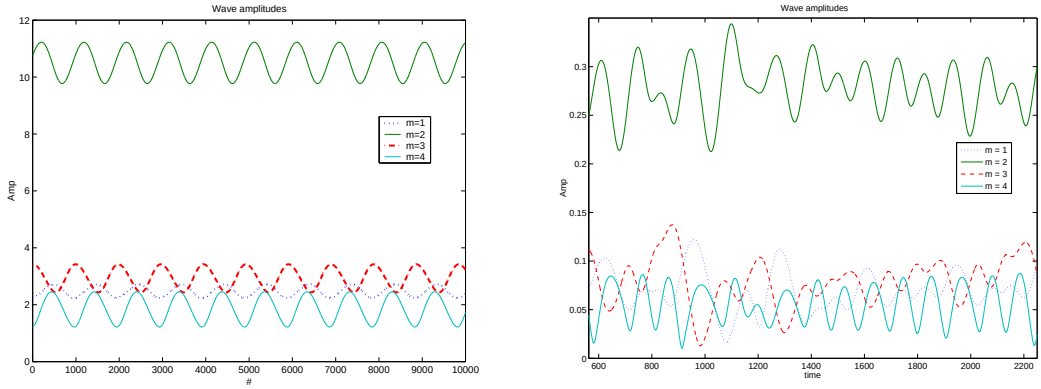

Figure 2: Typical time series of wave amplitudes for (a) and Amplitude vacillation and (b) a Modulated Amplitude vacillation. Quantities shown are Fourier amplitudes from the temperature fields calculated by the model described by *Randriamampianina and Crespo Del Arco* [68].

For laboratory experiments of baroclinic flows, these types of amplitude vacillations are contrasted to 'structural vacillation', 'tilted-trough vacillation' or 'shape vacillation' [32, 79, 64, 19, 30, 71, 17]. These flows are mainly characterised by distinct changes in the shape but little changes in the power of the waves. While these vacillations can occur at a distinct time scale, they tend to be much less regular than amplitude vacillations, and the time scale is shorter than that of the typical amplitude vacillation. *Hart* [22] also reported the phenomenon of 'frequency vacillation' in the mechanically-driven two-layer experiment which appeared to involve an oscillation of the wave speed independently of the wave amplitude though a similar time series was later interpreted by *Hart* [25] as 'wave number vacillation' where the flow structure vacillated between a mode 1 and a mode 2.

1.1. Nondimensional Parameters

In the thermally-driven baroclinic annulus, the two principal non-dimensional parameters are usually the Taylor number and the thermal Rossby number. The Taylor number,

$$Ta = \left(\frac{f\,L^2}{\nu}\right)^2 \frac{L}{d} = \frac{4\Omega^2\,(b-a)^5}{\nu^2 d}, \tag{1}$$

is essentially the ratio of the Coriolis term to viscous dissipation where $\Omega = f/2$ is the angular velocity of the annulus, L and d the horizontal and vertical length scales ($L = b - a$ with a the radius of the inner cylinder and b that of the outer), and ν the kinematic viscosity. Using an aspect ratio of $\gamma = L/d$, the Taylor number can be equated to the Ekman number as $Ta = \gamma E^{-2}$.

The thermal Rossby number,

$$\Theta = \frac{g\alpha\, d\,\Delta T}{\Omega^2\,(b-a)^2} \tag{2}$$

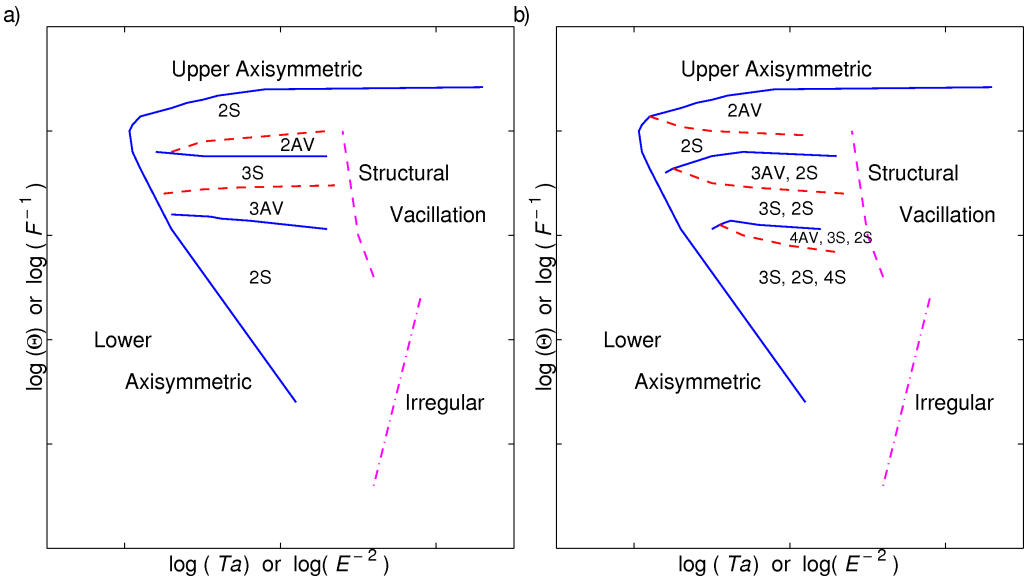

Figure 3: Illustration of typical regime diagrams for flow regimes in the thermally-driven baroclinic annulus, a) filled with air (after *Castrejon-Pita and Read* [7], *Randriamampianina et al.* [69] and *Read et al.* [72]) and b) filled with a water-glycerol fluid (after *Hide and Mason* [32] and *Hignett* [34]). The numbers refer to the dominant wave number and 'S' indicates a steady wave while 'AV' indicates amplitude vacillations including complex vacillations such as MAV. Common ranges of the values explored in such regime diagrams are $O(10^{-3}) \lesssim \Theta \lesssim O(1)$ and $O(10^5) \lesssim Ta \lesssim O(10^{10})$.

is a measure of the vertical stratification through a ratio of the buoyancy term over the Coriolis term. The term 'thermal Rossby number' originates from the standard Rossby number, $Ro = U/(fL)$ where the scaling velocity is defined through the thermal wind balance $U_{th} = g\alpha\Delta T\, d/(fL)$. The parameter is also related to the stratification through the buoyancy frequency, $N^2 = -(\partial\rho/\partial z)\, g/\rho$ (commonly also referred to as the Brunt-Väisäla frequency), and by that to the rotational Froude number, $F = (fL/(Nd))^2$ as $\Theta = 4/F$. In either case, the thermal Rossby number is a measure of the thermal forcing of the system whereas the Taylor number is a measure of the dissipation. The mechanically-driven two-layer experiments tend to use the Rossby number defined by the mechanically imposed velocity as one of the two principal parameters, and then either the Froude number or a dissipation parameter defined as $r = \sqrt{E}/Ro$.

The flow observations can then be summarised in regime diagrams in the parameter space defined by the two parameters. While the illustrations of the regime diagrams in figure 3 were derived from the thermally-driven annulus, the equivalent regime diagrams for the mechanically-driven systems will show similar features and structures. Since the regime diagrams intend to highlight the typical occurrence of amplitude vacillation-type flows, they were compiled from a wide range of experimental observations across different systems and hence do neither show more complex flows such as MAV flows nor show specific values of the nondimensional parameters, since they depend on other parameters as well, such as aspect ratios and the Prandtl number. Common ranges of the values explored in these regime are $O(10^{-3}) \lesssim \Theta \lesssim O(1)$ and $O(10^5) \lesssim Ta \lesssim O(10^{10})$

. Irrespective of precise values, a common observation is that amplitude vacillations, including AV and MAV, are found within the parameter space occupied by the regular and steady waves, whereas the less regular structural vacillation types are found at higher Taylor numbers or lower values of the dissipation parameter as the flow moves towards turbulent flow.

The classic Reynolds number as the ratio of the dissipation to the advection term is linked to the Taylor and Rossby numbers through $Re = UL/\nu = (U/fL)(fL^2/\nu) = Ro/E$. Identifying the thermal Rossby number with the Rossby number and $Ta = \gamma E^{-2}$, the Reynolds number can be written as $Re = \Theta\sqrt{Ta/\gamma}$ and lines of constant Reynolds number in figure 3 are lines with a slope of $-1/2$ with low Reynolds number values in the lower left corner and high Reynolds numbers in the upper right corner of the regime diagrams. Inserting the typical ranges for Θ and Ta results in a typical range of the Reynolds number as $O(1) \lesssim Re \lesssim O(5)$. As will be seen later on in Section 3.5, Eq. (4), the Ekman or Taylor number quantifies the dissipation through the Ekman layers which is proportional to the potential vorticity. The Reynolds number, on the other hand, quantifies the horizontal viscous diffusion and is proportional to the second derivative of the potential vorticity and hence highly dependent on the length scales of the flow structures.

1.2. Transition to Amplitude Vacillation

Amplitude vacillations tend to develop from their corresponding steady wave flow through a supercritical bifurcation as precursor to a mode transition to a different wave number. While the occurrence of structural vacillation appears to be determined more by dissipation, the onset of amplitude vacillation and mode transitions are more determined by the thermal forcing. Other factors known to affect the occurrence of amplitude vacillation are the tank geometry and the fluid's Prandtl number. An impressionistic synthesis of the various experimental reports by, in particular *Hide et al.* [33], *Jonas* [38], *Hignett* [34], *Pfeffer et al.* [61, 63], *Buzyna et al.* [6], *Sitte and Egbers* [74] and *von Larcher and Egbers* [80], suggests the following generalisation: *vacillations seem to be more prevalent in a wider and deeper annulus filled with a higher Prandtl number fluid.*

The fact that vacillation appears more easily in a wider gap could be a different phrasing of another observation, namely that amplitude vacillation tends to be seen more when the baroclinic wave has a relatively low wave number. *Hide and Mason* [31] showed that only a finite range of wave number can be observed, given by the ratio of the zonal wave length to the gap width,

$$\alpha = \frac{m\pi(a+b)}{(b-a)} \quad \text{as} \quad 0.25\alpha \leq m \leq 0.75\alpha. \tag{3}$$

The key difference between the regime diagram for a low-Prandtl number fluid ($Pr \lesssim 1$ in figure 3a) and for a high-Prandtl number fluid ($10 \lesssim Pr \lesssim 80$ in figure 3b) is the relative position of the vacillating regime. For a lower Prandtl number, a steady wave can develop an amplitude vacillation as the thermal forcing is reduced, prior to a transition to a flow with a higher wave number, while the onset of amplitude vacillation in a fluid with a higher Prandtl number is usually found when the thermal forcing and stratification is increased. While there is no experimental evidence for a systematic trend in low-Prandtl number fluids, it has been observed in many experiments that vacillation is rare in water

but becomes more widely observed at higher Prandtl numbers, to a degree where steady waves become rare as the Prandtl number reaches values in excess of 40. For example, the water-filled annulus of *von Larcher and Egbers* [80] only exhibited flow resembling amplitude vacillation in the region between the $m = 2$ and $m = 3$ dominated range in the narrow-gap annulus, whereas the annulus filled with a silicone fluid of *Pfeffer et al.* [63] appears to show always vacillating flows in the regular wave range.

Bifurcation studies in a high-Prandtl number fluid by *Read et al.* [71] have suggested that the onset of vacillation on increasing Θ is consistent with a Hopf bifurcation, and similarly *Randriamampianina et al.* [69] showed the same for the onset of amplitude vacillation in direct numerical simulations of a low-Pr fluid on decreasing Θ. The intermediate case was covered by *Sitte and Egbers* [74] who were able to show that both existed, a Hopf bifurcation from a steady wave 2 to a 2AV on decreasing Θ towards the $m = 3$ region and a Hopf bifurcation from a steady wave 3 on increasing Θ towards the $m = 2$ region. The region between these two bifurcation showed secondary bifurcations to chaotic modulated vacillations, each involving both modes, $m = 2$ and $m = 3$, but dominated by their respective original mode. While the hysteresis in the transition between modes involving only steady waves and amplitude vacillation is substantial, the transition between the 2-dominated and the 3-dominated chaotic flows seen by *Sitte and Egbers* [74] had little hysteresis and is more gradual, similar to the transition between complex amplitude vacillation flow observed by *Früh and Read* [17]. It appears that the modulated vacillations always involve activity in other modes, especially the sidebands of the dominant mode, and thereby facilitate the transition from one dominant mode to the next lower or higher mode.

In the corresponding two-layer experiment, *Hart* [22] observed that amplitude vacillation emerged from a steady wave when the driving of the lid and consequently the Rossby number was decreased. If the vertical velocity shear, either driven by the lid or through the thermal wind balance, is taken as the 'forcing' of the system, then the Rossby number defined by the lid rotation takes the equivalent role as the thermal Rossby number defined by the thermal wind. In that case, the observed transition from a steady wave to the amplitude vacillation in the two-layer system corresponds to the thermally-driven annulus filled with a low-Prandtl number fluid.

2. Mechanics of Amplitude Vacillation

In this section, some possible processes resulting in amplitude vacillation will be presented. As all observations suggest that AV is a global modulation of a finite-amplitude steady wave mode and that the steady wave originates from a global-mode instability of a zonal flow, the processes are usually expressed in terms of energy transfer between modes and the underlying zonal flow. In this framework, the energy is described in such terms as 'Zonal kinetic energy', 'Zonal potential energy', 'Eddy kinetic energy', and 'Eddy potential energy' [45]. Following *Hart* [24], the possible transfer routes can be illustrated as in Figure 4. In the mechanically driven two-layer system, the lid injects kinetic energy into the two fluids, which are then converted to a distortion of the interface, while in the thermally-driven annulus, the imposed horizontal temperature difference sets up the sloped isotherms and the vertical shear flow. In both cases, the baroclinic instability releases the zonal potential energy stored in the sloped isotherms or isopycnals and transfers this to eddy potential energy and then kinetic energy of growing wave modes.

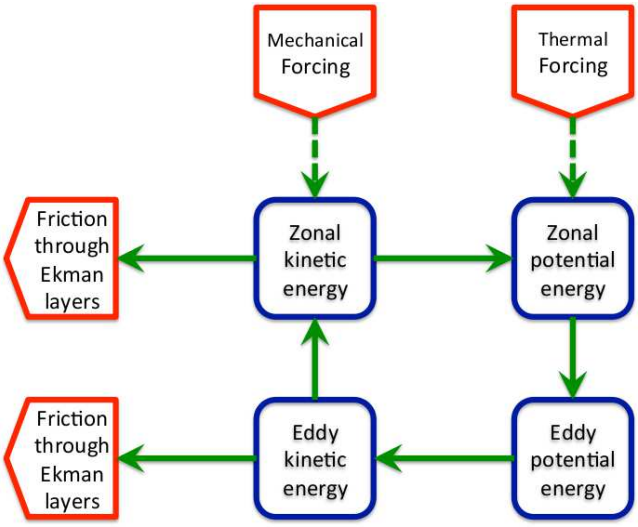

Figure 4: Illustration of the routes of energy transfer from the forcing of the vertical shear in the two-layer experiment, or from the imposed baroclinicity in the thermally-driven annulus to dissipation of the kinetic energy (adopted from Fig.6 of *Hart* [24], ©American Meteorological Society. Used with permission) and incorporating the thermal forcing relevant for *Pfeffer et al.* [61].

These lose energy through friction from the Ekman layers and through horizontal viscous diffusion but also feed back into the zonal flow. The feedback which can lead to an equilibration to a steady wave arises from the fact that the energy transfer from the eddies to the zonal flow reduces the baroclinicity until a balance between the energy supply from the forcing is balanced by energy loss through Ekman friction and diffusion.

Amplitude vacillation can set in when this balancing point of forcing and dissipation becomes unstable, and a slight increase in wave amplitude does not lead to a sufficient reduction in zonal potential energy and *vice versa*. *Pfeffer et al.* [61] used experimental data to test a suggestion by *Pfeffer and Chiang* [60] that the main energy conversion resulting in amplitude vacillation would be the two routes between zonal and eddy potential energy and between eddy potential and kinetic energy. The observations showed that the two potential energy terms were shifted by a quarter vacillation period, or phase-shifted by $\pi/2$, with the zonal potential energy leading. This means that the time of maximum zonal potential energy coincided with increasing eddy potential while the maximum eddy potential energy coincided with decreasing zonal potential energy. The results for the kinetic energy terms were noisier but suggested that they were coinciding with their respective potential energy terms or very slightly delayed. An idealisation of Figures 17 to 19 from *Pfeffer et al.* [61] in our Figure 5 illustrates the various energy terms in (a) and the main energy conversion terms in (b). A positive value in Figure 5 (b) corresponds to an energy flow in the direction given by the arrow in the annotation and a negative value indicates a reverse energy flow. In particular, Figure 5(b) shows that the energy transfer between the potential energy forms appears to be always from the zonal to the eddy potential energy, and that the transfer between the two eddy energies appears to be always from the eddy potential energy to the eddy kinetic energy. In contrast to this,

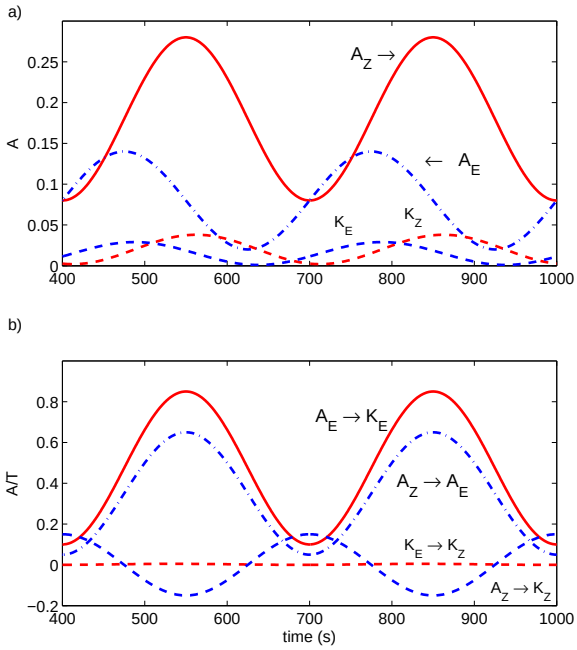

Figure 5: Idealisation of the energetics for an amplitude vacillation cycle (after *Pfeffer et al.* [61]) using A_Z for zonal potential energy, A_E for eddy potential energy, K_E for eddy kinetic energy, and K_Z for zonal kinetic energy. a) Energy contained in that type, b) rate of energy transfer from one type to another (adopted from Figures 17, 18 and 19 of *Pfeffer et al.* [61], ©American Meteorological Society. Used with permission) .

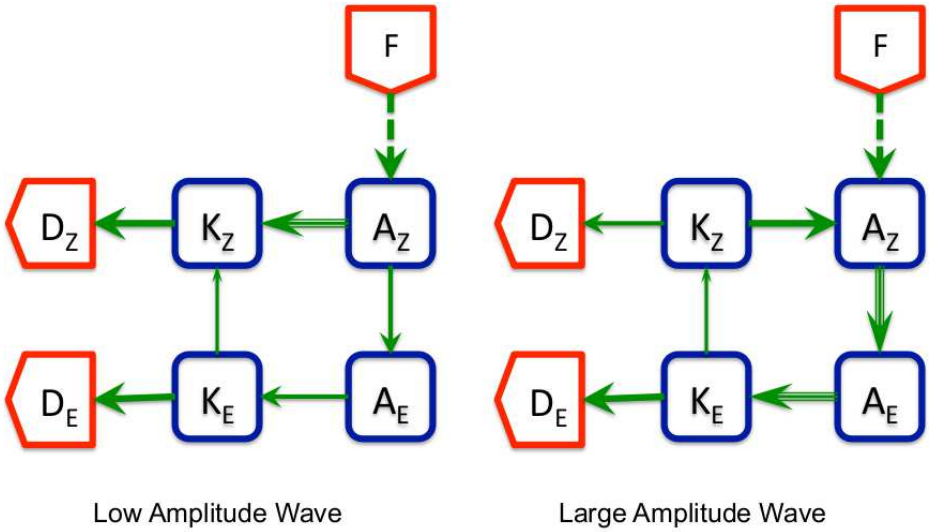

Figure 6: Schematic of the energy flow during the two extreme stages of an amplitude vacillation as calculated by *Pfeffer et al.* [61] using F for forcing, A_Z for zonal potential energy, A_E for eddy potential energy, K_E for eddy kinetic energy, K_Z for zonal kinetic energy, and D for dissipation (adopted from Figures 20 and 21 of *Pfeffer et al.* [61], ©American Meteorological Society. Used with permission).

the transfer between the two zonal energy forms changes sign: the zonal kinetic energy receives energy from the zonal potential energy during minimum energy transfer from the zonal potential energy to eddy potential and then to eddy kinetic energy. This then changes to a drain from the zonal kinetic energy to the zonal kinetic energy at times when the energy transfer from this zonal kinetic energy to the other forms of energy is large. The transfer between the two kinetic energy terms was always very small but appeared to be in the direction from eddy kinetic to zonal kinetic energy. The reversal of the energy transfer between the kinetic energy terms is illustrated in Figure 6.

3. Modelling Approaches

3.1. Computational Fluid Dynamics

Hignett et al. [35] succeeded in reproducing a realistic amplitude vacillation in the finite-difference Navier-Stokes model for the Oxford annulus filled with a fluid of Prandtl number of around $Pr \approx 13$ from *James et al.* [37] even at a relatively low resolution of 16 grid cells in the radial and vertical, respectively, and 64 in the azimuthal direction, using a stretched grid to resolve the boundary layers adequately. A later version of this model, now known as MORALS, was used by *Young and Read* [87] to construct a more detailed regime diagram for this apparatus and found very good agreement in the structure of the regime diagram, similar to that of Figure 3(b).

Lu et al. [51] developed a numerical model using finite difference discretization in the radial and vertical but a spectral representation in the azimuthal direction to model the larger Florida annulus with a relatively narrow gap and filled with a viscous fluid of Prandtl number 73 (experiment B in *Pfeffer et al.* [63]) and found good agreement, in

particular the fact that vacillating flows were extremely common and steady waves very rare. *Lu and Miller* [50] then analysed two particular vacillating cases, one classified as amplitude vacillation and the other as structural vacillation. In particular, they observed that the amplitude vacillation showed a clear oscillation of the relative phase of the wave in the lower part of the annulus compared to that of the upper part. Steady baroclinic waves have long been associated with a clear westward tilt of the temperature field and associated vertical heat transport, e.g. *Hide and Mason* [32]. With this in mind, the strong variation in the westward tilt is associated with the transfer between eddy kinetic energy (little tilt) and eddy potential energy (strong tilt) from the basic energy transfer model given in Figure 4. In contrast, the case classified as structural vacillation shows no such vertical tilt of the flow features but is essentially barotropic.

A high-resolution spectral Fourier-Chebyshev model of the thermal annulus filled with air was used by *Maubert and Randriamampianina* [52] with the then surprising observation that vacillating flows occurred on increasing the rotation rate (or the forcing towards favouring higher wave numbers). At the time this was surprising as all previous vacillation studies had been carried out in liquids where vacillation is found on decreasing the rotation rate. *Randriamampianina et al.* [69] then traced a full bifurcation sequence from the initial instability to a chaotic modulated amplitude vacillation which was subsequently confirmed experimentally by *Castrejon-Pita and Read* [7].

3.2. Quasi-Geostrophic approximation

In the quasi-geostrophic approximation, the momentum equations are scaled against the Coriolis term and then ordered in a series of terms of increasing power of the Rossby number, where the Rossby number is the ratio of the advection term to the Coriolis term, $Ro = U/(fL)$, e.g. [58]. If the Rossby number is small, the leading balance of forces is the Coriolis force to the horizontal pressure gradient which leads to the definition of the geostrophic stream function. The terms of order $O(Ro^2)$ then give an equation for the evolution, advection and diffusion of this geostrophic stream function.

Based on the quasi-geostrophic approximation, a variety of models have been developed, all of which center around wave mode perturbations for the horizontal motion around an idealised baroclinic basic state. The vertical structure of this baroclinic basic state could be continuous such as the Eady model [11] or the Charney model [8] or discrete such as Phillips' two-layer model [65]. The model can be used for high-resolution modelling for a systematic truncation to a low order, or for investigating the evolution of a specific perturbation.

3.3. Low-order Models

The picture of a flow with a regular spatial structure has led to a number of low-order dynamical systems models of amplitude vacillation in which the components are as follows:

1. A constant forcing, often represented as a constant vertical shear velocity, applied positively to a pair of wave mode amplitude equations,
2. A mean-flow correction equation, coupled to the wave amplitude (the larger the wave, the stronger the correction), which counteracts the forcing (applied negatively,

3. Dissipation applied negatively to both the wave amplitude and the mean-flow correction equations.

This suggests that the system requires at least three dimensions but the energy transfer routes indicated in Figure 4 suggests that four components are needed. Translating the amount of necessary information to a normal-mode decomposition, this would suggest a travelling barotropic wave (consisting of two modes or amplitude and phase), a travelling baroclinic wave (also two degrees of freedom) and a mean flow correction. While this adds up to five degrees of freedom it is recognised that one of the phases can be eliminated by a suitable coordinate transformation, leaving four degrees of freedom. Reducing this to only three degrees of freedom would only be possible if either the relative phase or the relative amplitude between the barotropic and baroclinic mode is constant.

3.4. Eady-type Models

The basic instability as developed by *Eady* [11] led to the formulation of the nonlinear dynamics of finite-amplitude waves driven by a linear vertical shear. *Weng et al.* [85] expressed the flow through a (nondimensional) stream function, $\phi = -yz + \phi' + \bar{\phi}$, where $-yz$ is the basic Eady profile, ϕ' the wave field, and $\bar{\phi}$ the mean flow correction which they then expressed in modes using $e^{ikx} \sin l\pi y$ for the horizontal component of the fields and $\sinh \mu z$ and $\cosh \mu z$ for the vertical structure. Using this, *Weng et al.* [85] followed a bifurcation scenario from the initial instability to a steady wave with the lowest radial ($\sin \pi y$) wave number, which then underwent a period-doubling bifurcation, followed eventually by the growth of the second radial mode, $\sin 2\pi y$, which is referred to a structural vacillation. However, while period-doubling has been observed in the two-layer experiment, the only well-documented period-doubling in the thermally-driven annulus was associated with strong stationary forcing due to an imperfection in the apparatus [17]. *Weng and Barcilon* [83] suggested that, while structural vacillation is due to the interference of two radial modes of the same zonal wave, amplitude vacillation is due to the interference of two vertical modes of the same zonal wave. This is in accord with the CFD results from *Lu and Miller* [50] who identified the vertical transport of energy associated with periodic changes in the vertical tilt of the wave structure during the vacillation cycle. *Weng and Barcilon* [84] added more zonal wave modes to the model but in a way which did not allow for wave-wave interactions. With this they demonstrated that wave-mean flow interactions alone are sufficient to give rise to wave number vacillation as well as amplitude vacillation and structural vacillation.

3.5. Two-layer Models

Two-layer quasi-geostrophic models are a standard tool in Geophysical Fluid Dynamics, e.g. *Pedlosky* [58], and can be formulated for the stream function in each layer or for the barotropic and baroclinic components. For example on a β-plane in the layer formulation with ψ_i with $i = 1, 2$ for the upper and lower layer respectively, the equations can be written as

$$\left\{ \frac{\partial}{\partial t} + J\left(\psi_i, \cdot\right) \right\} q_i = -\frac{r}{2} \nabla^2 \psi_i + \frac{1}{Re} \nabla^2 q_i \tag{4}$$

with

$$q_i = \nabla^2 \psi_i + \beta y + (-1)^{-i} F_i \left(\psi_1 - \psi_2\right)$$

$$
\begin{aligned}
i &= 1 \text{ for upper layer, } 2 \text{ for lower layer,} \\
\nabla &= \frac{\partial^2}{\partial x^2} + \frac{\partial^2}{\partial y^2} \\
J(\psi, q) &= \frac{\partial \psi}{\partial x}\frac{\partial q}{\partial y} - \frac{\partial \psi}{\partial y}\frac{\partial q}{\partial x} \\
r &= \frac{\sqrt{E}}{Ro} = \sqrt{\frac{\nu f_0}{D^2}}\frac{L}{U}, \text{ the dissipation parameter,} \\
F_i &= \frac{\rho_0 f_0^2 L^2}{g(\rho_2 - \rho_1) D_i}, \text{ the Froude number, and} \\
Re &= \frac{UL}{\nu} = \frac{1}{r^2\, Ro}, \text{ the Reynolds number.}
\end{aligned}
$$

The equivalent form for the barotropic component, $\psi_s = (\psi_1 + \psi_2)/2$, and the baroclinic component, $\psi_d = (\psi_2 - \psi_1)/2$ respectively, is for the barotropic component ('s' = 'sum')

$$
\begin{aligned}
&\frac{\partial}{\partial t}\nabla^2\psi_s + \beta\frac{\partial \psi_s}{\partial x} + u_s\frac{\partial}{\partial x}\nabla^2\psi_s + u_d\frac{\partial}{\partial x}\nabla^2\psi_d \\
&\qquad + J\left(\psi_s, \nabla^2\psi_s\right) + J\left(\psi_d, \nabla^2\psi_d\right) \\
&= -r\nabla^2\psi_s + Re^{-1}\nabla^4\psi_s
\end{aligned}
\tag{5}
$$

and for the baroclinic component

$$
\begin{aligned}
&\frac{\partial}{\partial t}\left(\nabla^2 - 2F\right)\psi_d + \beta\frac{\partial \psi_d}{\partial x} \\
&\qquad + u_s\frac{\partial}{\partial x}\nabla^2\psi_d + u_d\frac{\partial}{\partial x}\nabla^2\psi_s + 2Fu_d\frac{\partial \psi_s}{\partial x} \\
&\qquad + J\left(\psi_s, \nabla^2\psi_d\right) + J\left(\psi_d, \nabla^2\psi_s\right) - 2FJ\left(\psi_s, \psi_d\right) \\
&= -r\nabla^2\psi_d + Re^{-1}\left(\nabla^2 - 2F\right)\nabla^2\psi_d
\end{aligned}
\tag{6}
$$

followed by a suitable spectral expansion and truncation, for example Fourier modes for a straight channel [16]

$$
\begin{aligned}
\psi_{s,d} &= \sum_{n=1}^{N} \phi(t)_{s,d}^{n} \cos n\pi y \\
&+ \sum_{m,n=1}^{M,N} \left(\chi(t)_{s,d}^{mn} \cos\frac{2m\pi}{\alpha}x + \sigma(t)_{s,d}^{mn} \sin\frac{2m\pi}{\alpha}x\right)\sin n\pi y.
\end{aligned}
\tag{7}
$$

To satisfy the lateral boundary conditions, only some of the cross-channel Fourier modes are possible but the nonlinear interactions in the equations result in terms of the other modes and this energy must be projected onto those which do satisfy the boundary conditions. If the product of two wave terms has a zero zonal wave number, $m = 0$, it has a mean-flow structure of the form of $\sin n\pi y$ while the modes satisfying the boundary conditions are of the form $\cos \ell\pi y$. This means that each term of radial mode n has to be expressed by a series of zonal flow correction terms ℓ with

$$
c_{n\ell} = \frac{2}{\pi}\left(1 - (-1)^{n+\ell}\right)\frac{n}{n^2 - \ell^2}. \tag{8}
$$

The Reynolds-number term was originally omitted in the low-order models as it was assumed that the Stewartson layers at the side boundaries were 'passive' while the relevant dissipation occurred through Ekman suction from the Ekman layers as the horizontal boundaries. However, *Smith* [75] showed that the side boundaries are involved in the energy balance for the fluid interior and, in particular, that their absence resulted in a non-physical energy source of mean flow kinetic energy.

One of the earliest applications by *Lorenz* [47] of a truncation of a two-layer model to investigate specifically amplitude vacillation, arrived at a 14-dimensional system, capturing a barotropic zonal flow, a baroclinic zonal flow, and two different radial modes of a wave with a common zonal wave number, each represented by a cosine and a sine component of the stream function as well as a temperature component. Depending on the parameter values, this system produced steady wave solutions, periodic vacillations, as well as aperiodic flow which appeared to arise form a homoclinic bifurcation.

Further studies have successively reduced the dimension of the system to the absolute minimum required for vacillation to isolate a simple sufficient mechanism for vacillation. For example, *Pedlosky and Frenzen* [59], derived from the quasi-geostrophic two-layer equations a set of ordinary differential equations of the form

$$\frac{dA}{dt} = B - \gamma A \tag{9}$$

$$\frac{dB}{dt} = -\frac{\gamma}{2}\left(B - \gamma A\right) + A - c\left(A^2 + V_k\right) \tag{10}$$

$$\frac{dV_k}{dt} = \gamma\left(A^2 - \alpha V_k\right) \tag{11}$$

where A is the amplitude of the represented baroclinic wave, $B = dA/dt + \gamma A$, and V_k is a set of $k = 1 \ldots M$ cross-channel modes of the mean-flow correction to capture the mean flow correction adequately, cf eq.(8). In this model, only the wave amplitude is represented explicitly but not the phase speed.

Pedlosky and Frenzen [59] showed that this system can be reduced to a form equivalent to the classic Lorenz equations, originally derived as the simplest model for Rayleigh-Bénard convection [46]. The relationship between the Lorenz equations and the two-layer model equations was subsequently analysed and discussed by *Lovegrove et al.* [48].

4. Wave Interactions

4.1. Wave Triad Interactions

A common description of the underlying processes is to identify the transfer to and from the eddy kinetic and potential energies through nonlinear wave interactions which arise explicitly in the advection term, $(\mathbf{u}\cdot\nabla)\mathbf{u}$ of the Navier-Stokes or 'primitive' equations or the Jacobian $J(\nabla^2\psi, \psi)$ in the vorticity-stream function form of the momentum equations, when the flow field is expanded into Fourier modes. The product of sine and cosine terms leads to contributions to the equations for the modes with mode numbers of the sum and difference of the two terms in the product. This leads to the notion of *w*ave triads: two waves with zonal and radial wave numbers (m, n) and (m', n') combine in the multiplication to structures with wave numbers $(m'', n'') = (m \pm m', n \pm n')$ which then appear in the evolution equation for those respective modes. These possibilities are

constrained for two-dimensional and non-divergent flow such that energy has to flow to both, larger and smaller scales, in such a way that both kinetic energy and enstrophy are conserved [13]. In addition, *Hasselmann* [27] pointed out that within a triad only the wave with the highest frequency can support energy transfer to the other two members of this triad, which was confirmed experimentally by *McEwan et al.* [53]. Finally, the energy transfer to a mode will be most effective if the frequency of the forcing is equal or close to that of the wave itself ('resonance'). All these together then lead to the concept of resonant triads [5, 66], in which triads can interact if their frequencies align to maximise energy transfer form one scale to others, which is expressed in the selection criteria for the zonal and radial wave numbers,

$$\left.\begin{array}{rcl} m \pm m' \pm m'' & = & 0 \\ n \pm n' \pm n'' & = & 0 \end{array}\right\}, \tag{12}$$

respectively, and resonance condition for their frequencies

$$\omega - \omega' - \omega'' \ll \langle\omega\rangle\,, \tag{13}$$

where $\langle\omega\rangle$ is the average drift frequency of the three modes. True resonance is achieved if the left hand side is equal to zero but energy transfer can also take place at non-zero but small values. In a steady wave case, the nonlinear coupling would lead to entrainment of the frequencies such that they do add up to zero but in cases with varying mode amplitudes the strength of entrainment may also fluctuate. If the left hand side is non-zero when the coupling is weak, the waves may drift apart but if that drift is slow, i.e. $\ll \langle\omega\rangle$, their relative phases will still be close enough to re-establish entrainment when the amplitude of the driving mode becomes again strong enough.

The basic form of nonlinear interactions through a resonant triad is illustrated in Figure 7 in a diagram following *Ablowitz and Segur* [1, §4.2.b] using the dispersion relation for linear Rossby waves against the zonal wave number for the first three cross-channel modes. Here, the selection criteria are satisfied by choosing two wave modes and calculating the difference between the wave modes to identify candidates for triads. To determine whether there is the possibility for resonance, the difference in the frequency of the chosen pair of waves is calculated. The wave number difference and the frequency difference are then used to place the circle in the dispersion diagram. If a mode is found within that circle, it satisfies the condition and can participate in the resonant triad interaction. As the selection rule applies to both, the zonal and cross-channel wave number, the graph is in fact a projection of a three-dimensional graph with axes m, n, ω, where the lines for the different cross-channel modes are displaced in the third direction onto the plane of the zonal modes only. So, in this picture one has to ensure that the mode within the circle also satisfies the second of the selection rules in eq. 12. The example shown is the triad of zonal wave numbers 4, 3, and 1, where the two selection rules are satisfied. The resonance condition is not fully satisfied but still within a range allowing for some energy transfer. For this case, linear Rossby waves were used for illustration purposes. However, finite amplitude baroclinic wave have a substantially modified frequency. For one, the strongly nonlinear shape of a finite amplitude wave leads to the fact that a single wave mode is not represented by a single mode but by a superposition of the fundamental mode and its harmonics, all moving with the same group velocity. In addition the frequency or angular velocity of a wave depends on the wave amplitude. As

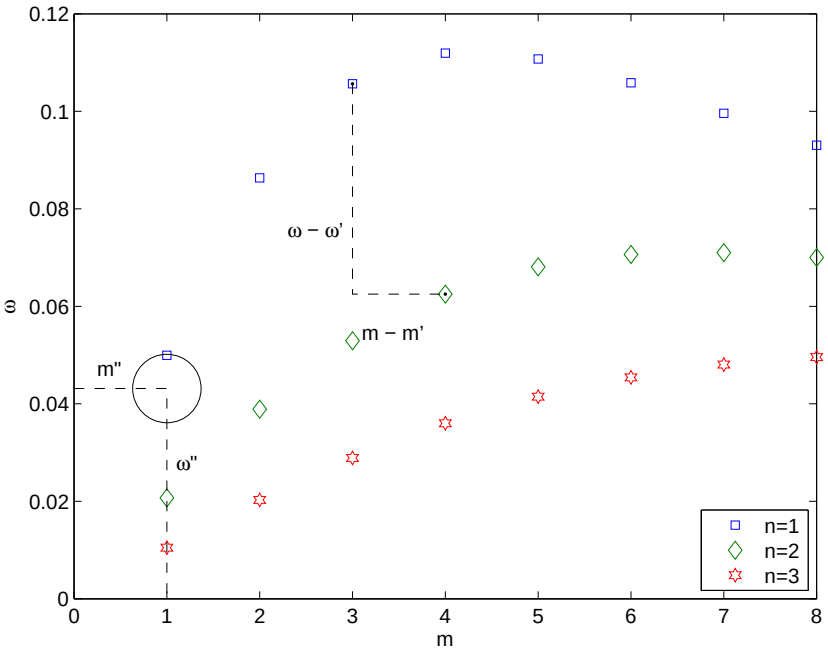

Figure 7: A basic routes of energy transfer through an almost resonant triads involving the first radial/cross-channel modes of wave numbers $(m, n) = (3, 1)$ and $(m', n') = (4, 1)$ and the second radial mode of wave number $(m'', n'') = (1, 2)$.

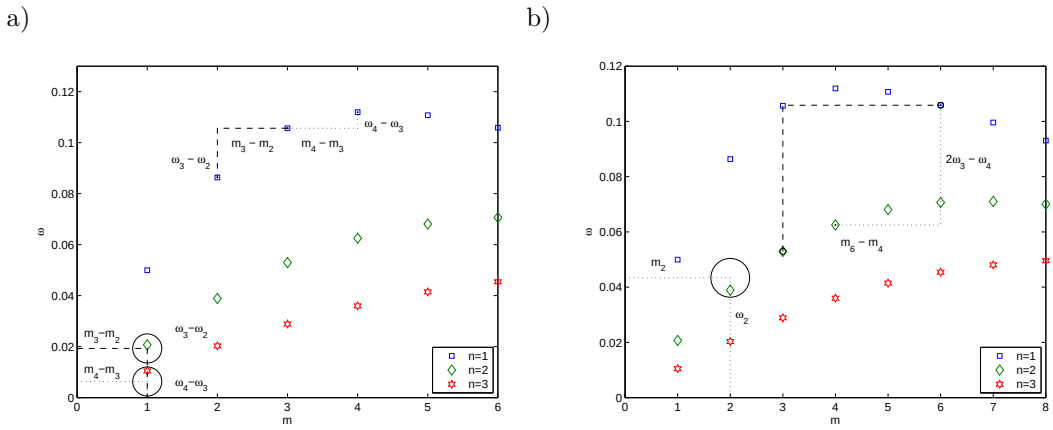

Figure 8: Two possible routes of energy transfer to the sidebands, either (a) involving two triads, coupled by the common long wave with $m' = 1$, or (b) through the harmonic of the dominant mode, $m' = 2m$.

a result, the resonance condition may be satisfied for a certain range of wave amplitudes but not for another.

4.2. Harmonic Forcing and Zonal Mean Flow Correction

One special case of the selection rules is where $m' = m$, in that case, the 'triads' are to feed energy to the first harmonic of the wave, $m'' = 2m$, and to the zonal flow, i.e. $m'' = 0$. To satisfy Fjørtoft's constraint of transfer to larger and smaller scales, the energy transfer to the harmonic requires the flow of energy from $(m, 2)$ to $(m, 1)$ and $(2m, 1)$. Since finite-amplitude waves are never sinusoidal, there is always strong energy transfer between a mode and its harmonic.

Similarly, for the mean flow correction, the transfer requires $(m, 1)$ and $(m, 2)$, though with the complication that the self-interaction is of the form of $\sin n\pi y$ while the modes satisfying the boundary conditions are of the form $\cos \ell\pi y$, cf. eq. 8. Since the resonance condition is irrelevant for the zonal mean flow, this route for energy transfer is always possible and only depends on the wave amplitude, whereas the energy transfer through resonant triads depends on the wave amplitudes and resonance conditions.

4.3. Higher-order Wave Interactions

If no triad is fully resonant, higher-order interaction scenarios can affect the baroclinic wave. One classic example of this is the Benjamin-Feir instability [4] where a monochromatic surface wave with wave vector $\mathbf{k}$ in a channel develops a slow modulation through the rise of a long wave of wave vector $\delta\mathbf{k}$ and 'side band' waves with wave vectors $\mathbf{k} \pm \delta\mathbf{k}$. As with the resonance condition for the resonant triads, eq. 13, a condition for the sideband instability can be written as [88]

$$2\omega_k - \omega_{k-\delta k} - \omega_{k+\delta k} = 0. \tag{14}$$

In the rotating annulus or two-layer experiments, the possible wave numbers are a discrete set, $k = 2\pi m/L$, and the longest possible wave is that with the wave number $m = 1$,

i.e. $\delta k = 2\pi/L$. With this, we can propose an illustration of how this sideband instability can occur through a coupled set of triads; one option invokes this long wave, $m' = 1$, while the other possible route involves the first harmonic of the main wave mode, as illustrated in Figure 8.

The questions which arise from this framework are: is any particular set of possible nonlinear interaction the essential process to destabilise a steady baroclinic wave and lead to amplitude vacillation? Do a range of interaction possibilities allow for all or specific types of amplitude vacillation.

4.4. Wave Interactions in Experiments and CFD

Hide et al. [33] developed a method to quantify the degree to which sidebands interact from spatially resolved temperature measurements in the thermally-driven rotating annulus. A Fourier analysis gave the amplitude, A, and phases, ϕ, of the zonal modes (but not resolving radial modes). Integrating eq. 14 suggests

$$2\phi_m - \phi_{m-1} - \phi_{m+1} \approx \text{const}$$

which lead to the definition of a side band phase locking function

$$\Phi_m = 2\phi_m - \phi_{m-1} - \phi_{m+1}, \tag{15}$$

and *Hide et al.* [33] observed that this phase locking function was indeed fluctuating around a constant value of $\Phi_m \approx \pi$ for fully-developed steady waves and amplitude vacillations. This did not hold for irregular flow nor for flows with a noticeable structural vacillation. The fluctuation around a constant value implies that the resonance would only be nearly satisfied and that nonlinear interactions couple the waves when they are strong enough, that the waves start to drift apart when that coupling becomes weaker as the main mode decays and that they become re-entrained when the wave grows again in the vacillation cycle. While the side band phase locking confirmed the presence of nonlinear wave interactions it does not distinguish between the two possible interaction routes illustrated in Figure 8. A theoretical study by *Plumb* [66] suggested the route through the long wave (Fig. 8a), while an analysis of a numerical simulation by *James et al.* [37] suggested the route through the harmonic (Fig. 8b).

4.5. Wave interaction scenarios in Low-order Models

Numerous studies have investigated the onset of vacillation in a range of low-order models, each of them isolating a few, or even a single, possible routes by which a steady, equilibrated wave starts to develop a vacillation. The most basic of them, for example, demonstrated that the wave-mean flow interaction between a single zonal wave and the mean flow is able to render a finite-amplitude steady wave unstable to vacillation if the forcing as quantified by the Froude number is large enough, or if the dissipation parameter, r, is small enough. As a comprehensive review of the earlier two-layer models by *Klein* [39] has shown, the 'interesting' behaviour of vacillating and chaotic flows in the simplest models with a single unstable wave of wave number (k, l) was mostly found at an intermediate balance of forcing and dissipation, as quantified by $r/\Delta^{1/2} = O(1)$, where $\Delta = F - (k^2 + l^2)/2$. *Klein* [39] also found that the inclusion of more wave modes into the models tends to stabilise the flow but that it does not fundamentally alter the types of flows observed.

Früh [16] analysed the various possible wave interaction scenarios in a set of low-order models where the included wave modes were carefully chosen to allow or suppress specific wave-wave interaction routes based on the selection criteria, eq. (12). For the analysis, the sideband phase locking function, eq. (14), was adapted to the triad resonance condition, eq. (13), to define a triad phase locking function. In the full model, they observed a sequence of bifurcations which, at least superficially, resembled the types of transitions found in the experiment, from a steady wave through an amplitude vacillation, to some forms of chaotic modulated amplitude vacillations, all of which involved substantial energy transfer between the different zonal wave modes, and finally to fairly irregular flow within the constraints of the dimensions of the system. All the flows involving more than one zonal mode showed clear resonant triad interactions, where the strength depended on the relative mode amplitudes. Removing specific triads from these model resulted only in moderate changes of the observed flows which suggested that the dynamics would make use of preferred triads if they are available but that they could make use of alternative routes for energy transfer. The results changed more substantially if all triads were removed and only wave-mean flow interactions were retained. In that case, the preferred route was through a competition between different zonal modes. This can be understood through the fact that the most unstable zonal mode is not usually the mode to which a flow would eventually equilibrate. The final steady-wave regime would usually be dominated by a lower zonal wave number [23, 26, 57]. For this reason, there is an amplitude-dependence of the growth rates of the waves such that a higher mode can grow preferably during a stage of strong zonal flow but that this mode suffers stronger damping and reduced growth compared to a longer wave when the zonal flow is reduced through the original growth of the shorter wave, leading to an alternation of which mode received more energy from the zonal flow.

5. Prandtl Number Effects

5.1. Observations

As discussed by *Lewis* [42], the Prandtl number as the ratio of the kinematic viscosity over the thermal diffusivity,

$$Pr = \frac{\nu}{\kappa}, \tag{16}$$

affects the first transition, from axisymmetric flow to regular waves. We have also already mentioned in Section 1 that the Prandtl number affects the transition to amplitude vacillation strongly in a way which can be summarised as follows: bifurcation to AV from a steady wave on decrease of Θ if $Pr \lesssim 1$, none or very little AV in water, onset of AV on increase of Θ if $Pr \gtrsim 10$ and amplitude vacillation prevalent if $Pr \gg 10$. One key characteristic defined largely by the Prandtl number alone is the relative thickness of the momentum and temperature boundary layers.

5.2. Possible Role of Boundary Layers

As the low-order models are, so far, all based on the quasi-geostrophic equations which do not solve explicitly the heat equations, nor the boundary layers, they rely on capturing the effect of boundary layers implicitly through Ekman suction from horizontal boundary layers and horizontal diffusion from vertical boundary layers. However,

the relative thickness of the thermal and velocity boundary layers affects the relative contribution to the heat transport through the boundary layers and through the fluid interior, respectively. A linear analysis by *Barcilon and Pedlosky* [3] identified that two parameters, namely the Ekman number and the product of the thermal Rossby number and Prandtl number, organise the relative contribution from different boundary layers into three scenarios,

Homogenous fluid, $Pr\Theta < E^{1/2}$: the fluid interior is homogeneous and constrained by the Taylor-Proudman theorem. Dissipation is through Ekman suction, and the sidewall boundary layers are the two Stewartson layers of thickness $E^{1/3}$ and $E^{1/4}$.

Weakly stratified, $E^{1/2} < Pr\Theta < E^{2/3}$: the Taylor-Proudman theorem is still strong but thermal stratification is increasingly noticeable. The $E^{1/4}$-Stewartson layer is largely unaffected but buoyancy very close to the wall affects the $E^{1/3}$-Stewartson layer and two new boundary layers develop: one very thin layer of thickness $E^{1/2}/(Pr\Theta)^{1/4}$ in which the viscous stresses balance buoyancy, and an outer, hydrostatic layer of thickness $(Pr\Theta)^{1/2}$.

Strongly stratified, $Pr\Theta > E^{2/3}$: the fluid is strongly stratified, the hydrostatic $(Pr\Theta)^{1/2}$ layer merges with the interior and only the $E^{1/2}/(Pr\Theta)^{1/4}$ buoyancy layer remains. Ekman suction is very weak and the interior is controlled by viscous diffusion.

Read [70] analysed the heat transfer calculated using the MORALS model (introduced above in Section 3.1) as function of a boundary layer ratio, defined as the squared ratio of the thermal sidewall boundary layer thickness to the Ekman layer thickness. This demonstrated that the Ekman layer was the limiting factor when the thermal boundary layer was wider than the Ekman layer but that the heat transport by the axisymmetric flow became constant when the thermal boundary layer became thinner than the Ekman layer.

5.3. Low-order model of wave - boundary layer interaction

Based on the scaling by *Barcilon and Pedlosky* [3] and the observations by *Read* [70] that the thinner of the two vertical boundary layers in a way determines the behaviour of the heat transfer in the steady wave through the Ekman layers and fluid interior, respectively, we can propose a simple conceptual model of the interaction between baroclinic waves and the thermal forcing of the Ekman circulation and the thermal wind in the interior using the following argument, which is also illustrated schematically in Figure 9.

Since the analysis by *Barcilon and Pedlosky* [3] suggests a change from the $E^{1/3}$ Stewartson layer to thermal boundary layers scaling with $Pr\Theta$, we use the $E^{1/3}$-Stewartson layer as our reference layer in the following argument which is based on the relative thickness of the vertical velocity and thermal boundary layers.

To determine the relative thicknesses and put these in the context of the non-dimensional parameters, a set of axisymmetric solutions of the MORALS code for a range of Prandtl numbers but otherwise fixed parameters was generated (see Appendix Appendix A for model specifications). Applying the classification from *Barcilon and Pedlosky* [3], all solutions presented here are nominally strongly stratified, with the transition from weak stratification to strong stratification at $Pr \sim 0.1$. Since the Ekman number was a constant in all computations, the $E^{1/3}$-Stewartson layer thickness was used as our reference

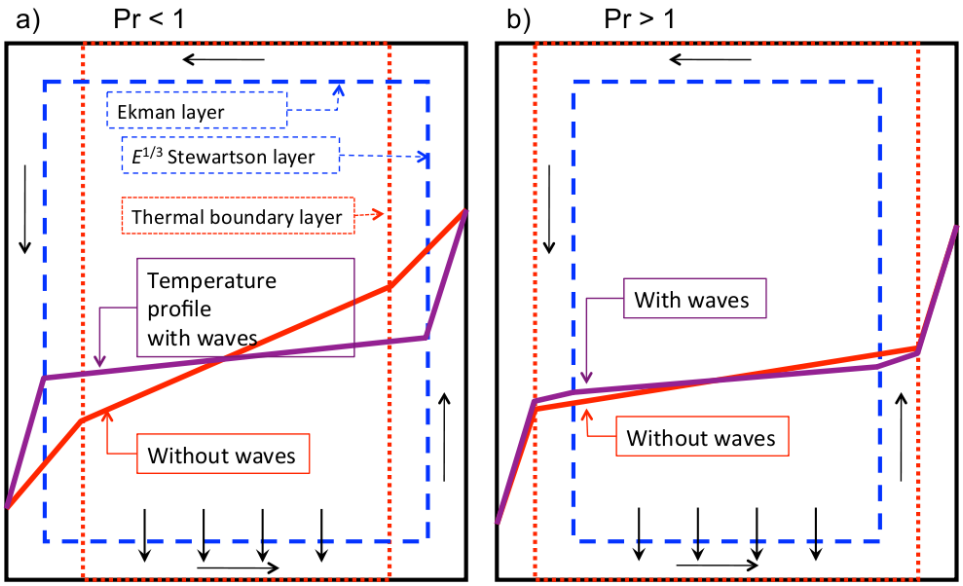

Figure 9: Schematic diagram of the effect of baroclinic waves on the mean radial temperature profile for a) $Pr < 1$ and b) $Pr > 1$. Shown are sections in the $r - z$ plane with cooling at the right wall, heating at the left, and insulated rigid upper and lower boundaries.

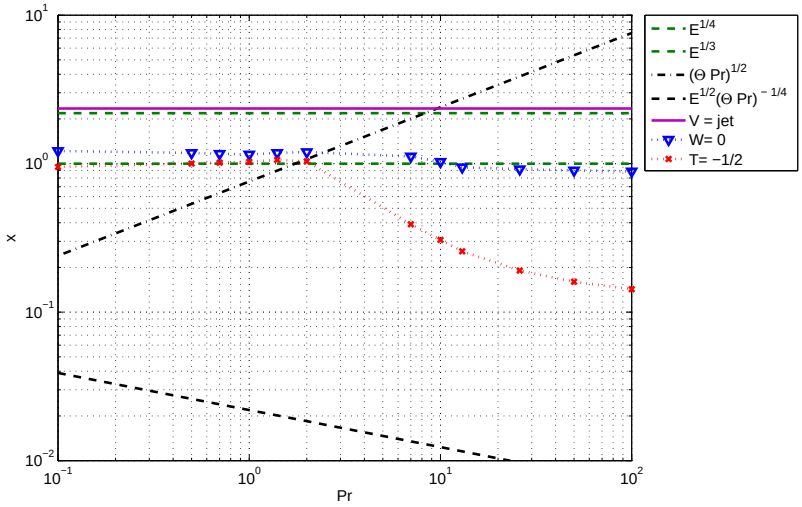

Figure 10: Comparison of boundary layer thicknesses obtained from axisymmetric solutions of the MORALS code with the theoretical Stewartson layer thicknesses and thermal layer thicknesses against Prandtl number. The thickness variable is scaled against the $E^{1/3}$-Stewartson layer.

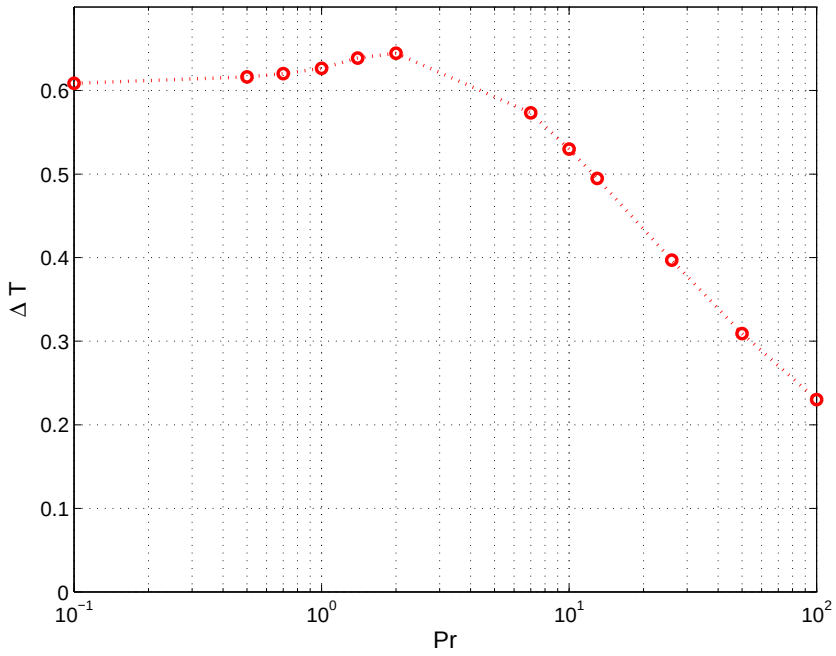

Figure 11: Effective temperature contrast across the fluid interior against Prandtl number, obtained from axisymmetric solutions of the MORALS code.

layer. Figure 10 shows the distances of the theoretical and computed boundary layer thicknesses at the inner cold wall. There the theoretical two Stewartson layers are shown as the horizontal green dashed lines and the location of the maximum jet velocity in the interior is shown as the solid line, while the outer hydrostatic thermal boundary layer is the black solid line and the inner buoyancy layer is the dashed black line. The extent of interior baroclinic flow is measured as the location of the maximum velocity of the baroclinic jet. This is located just outside the outer $E^{1/4}$ Stewartson layer and did not appear to depend on the Prandtl number at all. Since the axisymmetric solutions always showed a strong downwelling at the cold sidewall adjacent to a small upwelling (and *vice versa* at the warm wall), the extent of the vertical flow is measured as the location of zero vertical velocity and shown as the blue triangles with the dotted line. This is clearly limited by the inner $E^{1/3}$ Stewartson layer. To obtain a measure of the thermal boundary layer, the distance from the wall where the temperature had increased from $-\Delta T/2$ to $-\Delta T/4$ relative to the mean temperature was found. This is shown by the red crosses and dotted line. For $Pr \lesssim 2$ this thermal layer has a constant thickness which appears to be limited by the vertical convection since it is very close to the edge of the velocity boundary layer. Once the Prandtl number increases beyond $Pr \sim 2$, the temperature gradient near the walls increases noticeably and follows a decay similar to that of the buoyancy boundary layer. The change-over from a solution where the heat transfer is limited by the velocity boundary layer to that where the thermal boundary layer thickness affects the heat transfer occurs at a point where the theoretically derived hydrostatic $(Pr\Theta)^{1/2}$ layer becomes thicker than the $E^{1/3}$ Stewartson layer. With this, we can now state the principle of the Prandtl number dependent coupling between the boundary layer and the baroclinic waves as:

1. The horizontal temperature profile across the entire domain is characterised by high temperature gradients within the thermal boundary layers and smaller gradients outside of them.
2. The velocities behaviour is split into velocity boundary layers and the 'fluid interior'. The 'interior' is defined by the horizontal velocities and is therefore terminated by the $E^{1/3}$ Stewartson layers.
3. The effective forcing of the thermal wind in the fluid interior is determined by the horizontal temperature difference across the fluid interior.
4. Therefore the temperature at the top of the $E^{1/3}$ Stewartson layers determines the thermal wind. The ratio of the effective temperature contrast over the imposed temperature contrast as a function of the Prandtl number for axisymmetric flow derived from MORALS results is shown in Figure 11.
5. Finite-amplitude baroclinic waves, at least those with a wave number preferred by Hide's geometric constraint, eq. (3), tend to fill the gap up to the edges of the Stewartson layers.
6. Finite-amplitude waves enhance the heat transfer through the interior, and thereby act to reduce the temperature gradient within the fluid interior.
7. If the thermal boundary layers are thinner than the Stewartson layers, the temperature at the edges are affected only slightly since most of the imposed temperature contrast is taken by the thermal boundary layers. Hence the feedback between sidewall forcing and baroclinic waves is minor

8. If, on the other hand, the thermal boundary layers are thicker than the Stewartson layers, the temperature at the edges of the boundary layers are affected substantially because the baroclinic waves extend to within the thermal boundary layers and thus provide an additional heat transfer route across the annulus directly from one thermal boundary to that at the opposite side wall.

This principle can be formalised in a one-dimensional model for the temperature at the interface between the Stewartson and the fluid interior based on the vertical heat convection through the Ekman circulation, the radial heat conduction, and the radial heat convection which is a function of the wave amplitude. If the radial extent of the fluid interior is taken to extend from $y = \pm 1$ with $y = 0$ at the centre of the annulus gap, the $E^{1/3}$-layer has a thickness of δ, and the nondimensional temperatures at the side walls are $T = \pm 1$, then the energy equation

$$\frac{\partial T}{\partial t} = -\mathbf{u}\cdot\nabla T + \frac{1}{Pr}\nabla^2 T$$

can be discretised for the temperature at the interface, $T(y) = \theta$ as

$$\frac{\partial \theta}{\partial t} = -v_w \frac{\theta}{1} - w_s \frac{1-(-1)}{\gamma_v - (-\gamma_v)} + \frac{1}{Pr}\frac{(1-\theta)/\delta - \theta/1}{1+\delta/2-1/2}$$

where $v_w\theta$ is the heat convection into the interior through the waves with a radial fluid velocity v_w, w_s/γ_v its the vertical heat convection through the Stewartson layer with a vertical velocity of w_s. The parameter γ_v is the vertical aspect ratio of the annulus. The last term is the horizontal heat conduction from the wall (at $y = 1+\delta$) to the edge of the boundary layer at $y = 1$, and from that edge to the centre of the annulus at $y = 0$. One implicit assumption here is that the flow and temperature fields are symmetric around the centre line. This can then be re-arranged to a differential equation with a constant term, a term proportional to the effective temperature, θ, and a term proportional to the strength of the baroclinic waves as quantified by v_w.

$$\frac{\partial \theta}{\partial t} = \frac{2}{Pr(1+\delta)\delta} - \left(\frac{2}{Pr\ \delta} - v_w\right)\theta - w_s\frac{1}{\gamma_v}. \tag{17}$$

Coupling this equation to a low-order two-layer model can then simulate the effect of the now wave-dependent effective thermal forcing from the edge of the Stewartson layer. An implementation of this into the minimal two-layer model of a single wave and a single mean-flow correction term by *Lovegrove et al.* [49] is presented in Appendix Appendix B. Some initial results of this are shown as a set of bifurcation diagrams for a selection of Prandtl numbers in Figure 12 where the Taylor number was kept fixed at $Ta = 10^5$ and the bifurcation parameter was the thermal Rossby number. The diagrams show the mean and extreme values of the wave amplitude of the barotropic component, $\sqrt{\chi_s^2 + \sigma_s^2}$ with χ_s the barotropic cosine mode and σ_s the sine mode, following the convention used in Eq. (7) for either increasing Θ (left branch) or decreasing as a test for hysteresis. In general, the axisymmetric flow develops into a steady wave on increasing Θ, then develops an amplitude vacillation before returning to the axisymmetric flow. The main feature of Figure 12 is that the location of the steady waves and the amplitude vacillation shifts towards higher Θ as the Prandtl number is increased. Furthermore, the relative

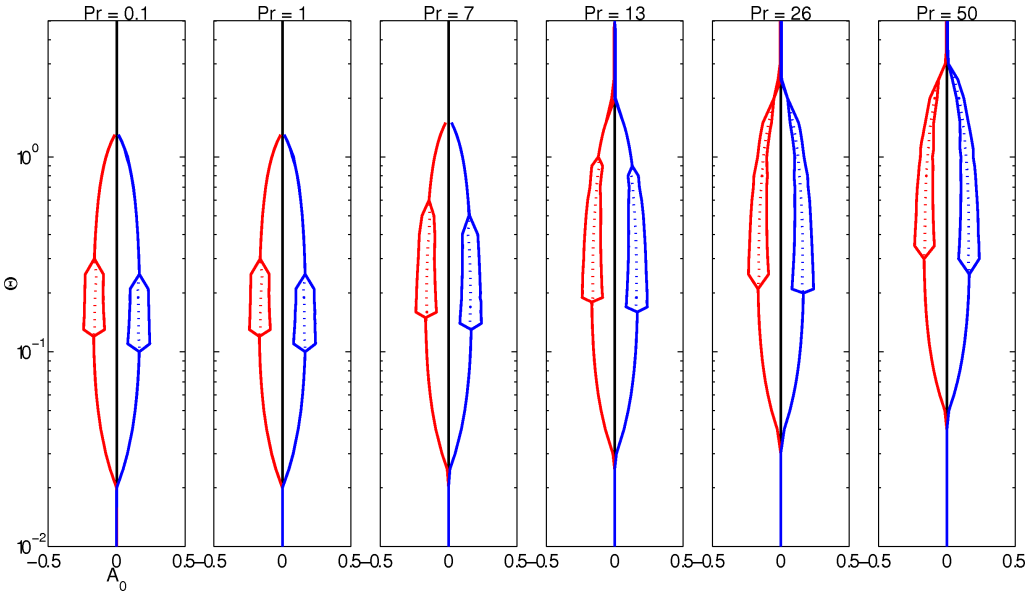

Figure 12: Bifurcation diagrams for $Ta = 10^5$ and various 'Prandtl numbers' with the thermal Rossby number, Θ as the bifurcation parameter. The quantity plotted is the amplitude of the mean flow correction, on the left of the central axis for increasing Θ and on the right of the axis for decreasing Θ. The solid lines indicate the range of the amplitude and the dotted lines the mean amplitude.

extent of the steady over the vacillating flows shifts towards more prevalent vacillation for higher Prandtl numbers which is consistent with the experimental observations. The clear reversal of the bifurcation order is not captured in this very simple model, although a very small steady wave regime can be observed for the lowest Prandtl number above the vacillating regime.

In conclusion, there is some evidence that the proposed feedback between wave amplitude and the effective thermal forcing can contribute to the vacillation as seen in experiments, though this very simple model is far from complete.

6. Other Forms of Vacillation

6.1. Interference and Wave Number Vacillations

Though not strictly speaking an 'amplitude vacillation', it is worth to mention the processes explaining the interference vacillation found in the two-layer experiment. Following on from the concept of the onset of a wave through a Hopf bifurcation, *Ohlsen and Hart* [55] used the two-layer model developed for the two-layer experiment to investigate the dynamics following a double-Hopf bifurcation where two modes become unstable simultaneously. They found that the two modes can both grow to a finite amplitude. These two co-existing modes can then generate zonal-flow oscillations through interactions of a mode with its sidebands. Interference vacillation was also found by *Harlander et al.* [21] in the thermally driven annulus with a free surface. In contrast to the two-layer experiment, there was no indication that the two waves were coupled through nonlinear

interactions but they appeared to be a linear superposition of two modes of different zonal wave number drifting at different speeds.

Related to amplitude vacillation is the wave number vacillation as it arises from the interaction between two or three wave modes and the zonal flow. *Weng and Barcilon* [84] suggested that the two-wave wavenumber vacillation arises from an imbalance in the forcing of the wave from the baroclinic zonal flow and viscous damping of the two participating unstable modes.

6.2. Structural Vacillation

Over the year, many processes have been invoked to understand the nature of 'structural vacillation' and the transition to it. Key features of structural vacillation compared to amplitude vacillation is that smaller horizontal scales are involved besides the dominant wave mode and that the vertical structure is much less baroclinic. The more barotropic nature of this flow was observed experimentally by *Pfeffer et al.* [62] and subsequently confirmed through CFD for those cases by *Lu and Miller* [50] and for the air-filled annulus by *Read et al.* [72]. Furthermore, the timescale associated with the structural vacillation is usually considerably shorter than that of an amplitude vacillation, though still longer than the rotation period of the apparatus. A systematic experimental study by *Tamaki and Ukaji* [79] suggested that the onset of structural vacillation occurs at a fairly well-defined place in parameter space irrespective of which wave mode dominates the flow which is in distinct contrast to the amplitude vacillation where its onset depends on the wave number of the flow. *Read et al.* [71] and *Früh and Read* [17] noticed that the overall heat transfer fluctuates only slightly compared to that of amplitude vacillations, another hint that the processes driving the onset of structural vacillation are fundamentally different from those leading to amplitude vacillation.

A closer analysis of the structural vacillation found by *Read et al.* [72] and *Früh et al.* [19] is presented here in terms of the temporal and radial spectra of the fluctuations relative to the steady wave. The azimuthally averaged temporal spectra are shown in Figure 13 as a contour plot in the radial-frequency plane, where the radial co-ordinate is the node number i from the computational grid with $r_i = \cos(i\pi/N), i = 1 \dots N$, as described by *Randriamampianina and Crespo Del Arco* [68] in this book, which stretches the radial coordinate to resolve some scales near the boundary. To show the key distances, the dashed lines indicated the near-wall region, within 1% and 5% of the gap width and the inner $E^{1/3}$ and outer $E^{1/4}$ Stewartson layers. The key regions of variability are located in the fluid interior but even more so in the outer Stewartson layers at the longer time scale of 32 nondimensional time units ($t = 2\Omega t^*$). This period, of around 10 rotation periods of the apparatus is consistent with the usually observed vacillation periods of structural vacillation. Additionally there is also a source of much faster fluctuations within the near-wall regions at a time scale of only 3 to 5 time units, of the same magnitude as the rotation period of the annulus. This suggests that a relatively fast boundary layer process might be involved in the onset of structural vacillation whereas amplitude vacillation was understood as a global instability of the fluid interior. The azimuthal spatial spectrum, in Figure 14 shows the clear peaks of the dominant mode 2 and its harmonics superimposed on a general decay with a decay rate between $p_\theta \sim m^{-2.2}$ and m^{-3}, which would be consistent with a quasi-geostrophic turbulence spectrum [9, 81]. The radial spectrum, on the other hand shows a spectrum with radial wave number as $p_r \sim k^{-5/3}$ which is closer to a mesoscale energy spectrum in terms of the horizontal wave

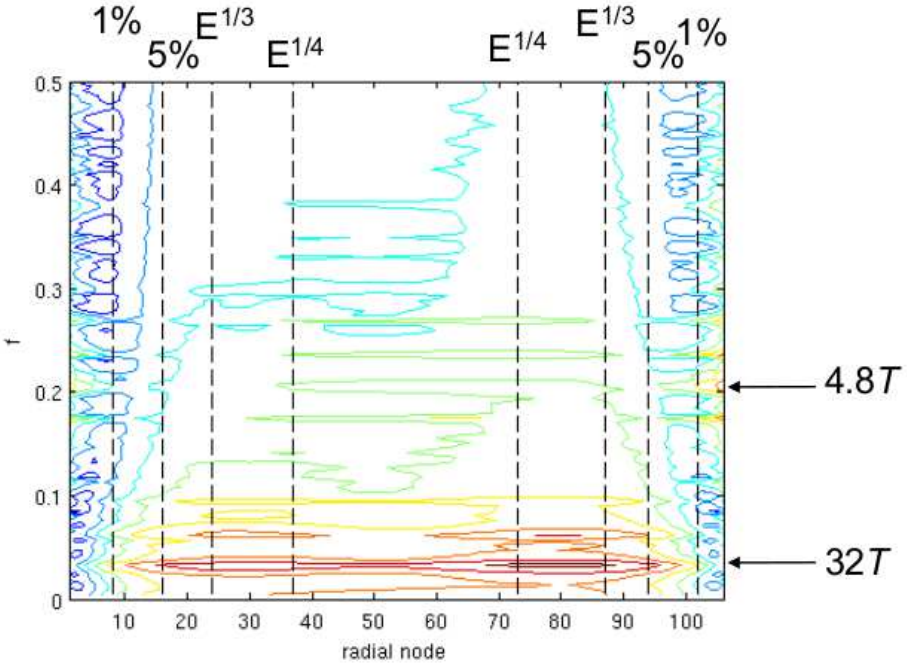

Figure 13: Radius-frequency contour plot of azimuthally averaged power spectral magnitude for structural vacillation in air-filled annulus.

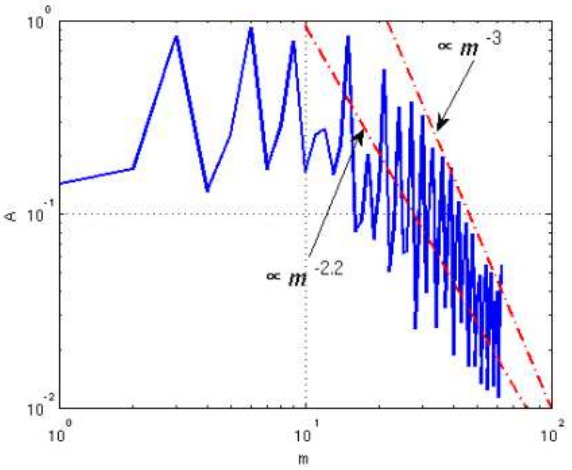

Figure 14: Azimuthal spatial spectrum, averaged over time and radius for structural vacillation.

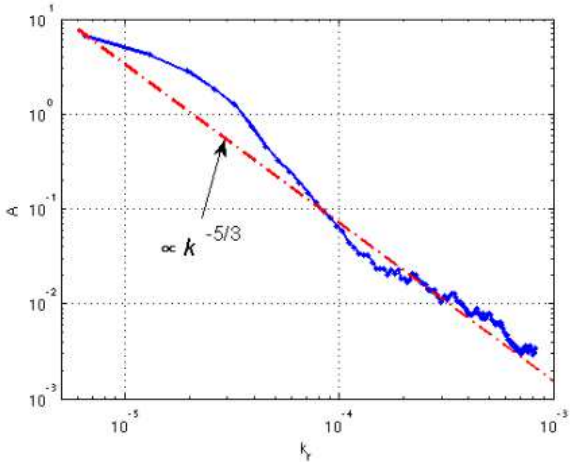

Figure 15: Radial spatial spectrum, averaged over time and azimuth for structural vacillation.

number [54] or strongly stratified turbulence where strong small-scale static instability is present [43].

One suggested route is the instability of a higher radial mode of the dominant wave growing to a finite-amplitude modulation of that higher mode superimposed on the still steady fundamental radial mode of that wave is supported by the experiments of *Früh and Read* [17] and explained in a low-order Eady-type model by *Weng et al.* [85]. This explanation would suggest that there is a clear bifurcation route from steady wave to AV which then bifurcates to a SV in some way. However, this bifurcation remains elusive, and calculations of the Grassberger-Procaccia dimension of amplitude vacillations and structural vacillations has repeatedly shown that amplitude vacillations are well behaved and appear to follow low-dimensional dynamics whereas the dimension estimates for measurements from structural vacillations do not converge to a reliable estimate [20, 71, 17]. Another explanation might be a localised instability of the large-amplitude wave resulting in possibly a barotropic instability of the type of a detached shear layer [18] but localised in space along the edges of individual wave lobes, or in the form of a breaking wave leading to internal gravity waves such as those described by *Jacoby et al.* [36]. Yet another option might be a boundary layer instability as the large-amplitude wave impinges on the sidewalls, such as seen by *Read et al.* [72] and *Früh et al.* [19].

7. Amplitude Vacillation as a Step towards Chaos and Turbulence

In this context, the distinction between 'chaos' and 'turbulence' is based on the assumption that chaotic flow is governed by deterministic equations which can be modelled by a finite (hopefully small) number of degrees of freedom whereas turbulence requires so many dimensions that it might, from a practical point of view, be as well an infinite-dimensional system or a non-deterministic system.

To distinguish these two cases, the attractor dimension reconstructed from experimental or numerical data can be used as a guide. So far, chaotic modulated amplitude

vacillation and similarly complex forms of amplitude vacillation have always appeared to follow fairly low-dimensional dynamics when their Grassberger-Procaccia dimension was estimated, as demonstrated for the thermally-driven annulus by *Guckenheimer and Buzyna* [20], *Read et al.* [71], *Früh and Read* [17] and *Sitte and Egbers* [74]. From all studies, it is clear that amplitude vacillation is a key candidate to explore a number of standard bifurcation scenarios through secondary Hopf bifurcations, Period-doubling cascades, and intermittency-type bifurcation, to name but a few. The majority of the evidence points to a picture whereby the chaotic flow is in some way the result of global mode instabilities or through attractor crises arising from two coexisting attractors associated with different zonal global wave modes. Either type of transition was always found to lead to strictly low-dimensional behaviour where the Grassberger-Procaccia dimension tended to be less than 4. Ultimately, the chaotic flow is normally terminated by steady wave flow again, usually of a lower wave number if $Pr > 1$ and a higher wave number if $Pr < 1$.

Another possible progression is to a structural vacillation. The evidence, however, points to an understanding that AV and SV are fundamentally different types of flow, and that a transition from AV to SV occurs more by accident than through a systematic transition. This is because the transition is only found at high Prandtl number where AV is so ubiquitous in the regular wave regime that it is virtually the only possible regular wave flow on which an SV can develop, whereas SV does also develop on a steady wave through an, as yet, poorly understood mechanism.

The transition to turbulence, on the other hand seems to be closely linked to either structural vacillation through the emergence of possibly localised flow structures, as the Taylor number is increased, or to the progressive emergence of higher wave modes as the rotation rate is increased (simultaneous increase of Ta and Θ). A re-evaluation of the dimension estimates for structural vacillation from [20] by *Pfeffer et al.* [64] supports the proposition that structural vacillation represents a secondary instability on top of the remaining stable baroclinic wave which gradually gains predominance as the flow becomes turbulent. Their argument is based on the observation that, at the onset of SV, the dimension estimates suggest a Grassberger-Procaccia dimension of 1.6, a number which persists as 'the answer'. At the same time a second scaling region develops at smaller scales in phase space. That second scaling region suggests a dimension of between 7 and 10, with an estimated dimension of full geostrophic turbulence of 11. These observations are consistent with those of *Sitte and Egbers* [74] and *Früh and Read* [17] who observed two scaling ranges for their weak structural vacillation, one suggesting a dimension of 1.3, the other 4.5. Complementary dimension estimates for the integrated total heat flux measured simultaneously with the temperature measurements in the same experiment gave inconsistent results with a suggested dimension of 5.8. Usually the heat transfer dimension, D_Q, would be related to that from the temperature data, D_T, as $D_Q = D_T - 1$ since the total heat transfer does not resolve the spatial structure within the flow. To overcome the difficulties presented by dimension estimates and spurious Lyapunov exponents, *Pfeffer et al.* [64] used Lorenz analog diagrams to visualise the degree of chaos by presenting the phase space distance between subsequent states to show how the apparently stable global flow structure is being broken up by spatially separated fluctuations.

8. Conclusions

This review of amplitude vacillation has attempted to introduce a range of methods to investigate this phenomenon, from careful experimentation in a thermally or a mechanically driven apparatus, complemented by high-resolution Computational Fluid Dynamics as well as targeted low-order models. By combining the findings from the various approaches it has been possible to build up a fairly comprehensive picture of the processes leading to, and involved in, amplitude vacillation. The main processes remain nonlinear wave-wave interactions and wave-mean flow interaction but also feedback mechanisms between the fluid interior and the boundary layers.

This survey has re-iterated the fact that the baroclinic annulus and the two-layer experiment are key fluid experiments to investigate a rich variety of nonlinear dynamics including chaotic flows and geostrophic turbulence. The success but also the challenges in modelling the observed flows successfully in CFD models makes this system a good candidate for model development and validation. For straightforward code validation it is possible to find relatively simple flows which are (or should be!) easy to model, and for model development there is the option to model slightly more complex flows which involve either a higher resolution or combine new processes such as gravity waves. It is also possible to push the experimental conditions to truly complex flows which are likely to remain a serious challenge to computational modelling.

From a practical point of view, a frequently asked question is how this experiment can possibly help to understand real atmospheric flows, let alone help to predict weather and climate more accurately. This is a valid question, especially as the boundary layers are much more important in the laboratory than in the atmosphere. Furthermore, atmospheres do not have the Stewartson layers to contend with and therefore should not be affected by the Prandtl number in the way as described in §5. However, through developing some understanding of how the Prandtl number affects the annulus flow it is possible to disentangle the laboratory-specific dynamics from those which are relevant to atmospheric or oceanic dynamics and to the atmospheric modeller.

Acknowledgments. The author wishes to thank in particular Raymond Hide, Peter Read, Patrice Klein, Christoph Egbers and Thomas von Larcher for many inspiring discussions on the baroclinic annulus and the concept of vacillation.

Appendix A. MORALS code set-up

The 2-D solver of MORALS was set up for axi-symmetric flow integration with a grid resolution of 24 by 24 and 32 by 32 without any appreciable difference, where the grid was stretched using a hyperbolic tangent function. As a result no further grid refinement was carried out.

The dimensions of the annulus were an inner radius of $a = 2.5$cm, outer radius $b = 8$cm, depth $d = 14$cm, and the temperatures were 18°C at the inner wall and 22°C at the outer wall.

The fluid properties at the reference temperature of $T_0 = 22$°C were a density of $\rho_0 = 1.043\text{g/cm}^3$, a kinematic viscosity of $\nu_0 = 0.0162\text{g/cm}^3$ and a thermal diffusivity, κ_0, calculated to set the Prandtl number as

Pr	0.1	0.5	0.7	1	1.4	2
κ_0	0.162	0.0324	0.0231	0.0162	0.01157	0.00810
Pr	7	10	13	26	50	100
κ_0	0.00231	0.00162	0.00129	0.000623	0.000324	0.000162

The variation of the fluid properties with temperature were a volume expansion coefficient for the fluid of $\alpha = 3.07 \times 10^{-4}\mathrm{K}^{-1}$ and quadratic approximations as

$$\begin{aligned}
\rho &= \rho_0 \left[1 - \alpha\,(T - T_0) - 7.83 \times 10^{-6}\,(T - T_0)^2\right] \\
\nu &= \nu_0 \left[1 - 2.79 \times 10^{-2}\,(T - T_0) - 6.73 \times 10^{-4}\,(T - T_0)^2\right] \\
\kappa &= \kappa_0 \left[1 - 2.33 \times 10^{-3}\,(T - T_0)\right].
\end{aligned}$$

Appendix B. Low-order model of boundary-layer feedback

The model to couple the one-dimensional boundary layer model with a single zonal baroclinic wave mode with zonal mode m and radial mode $n = 1$ was formulated to simulate the behaviour for annulus parameters given by

γ_h , the horizontal aspect ratio, $\pi(a + b)/(b - a)$

γ_v , the vertical aspect ratio, $L/(b - a)$

n , the zonal wave number

Pr , the Prandtl number, eq.(16)

Ta , the Taylor number, eq.(1)

Θ , the thermal Rossby number, eq.(2)

$\beta = df/dy$, the β effect

Defining equivalences between the thermally driven annulus and the two-layer system by using the thermal wind as the definition for both, the Rossby number of the two-layer system and the shear forcing, we can associate the two-layer terms on the left hand side with thermal annulus parameters on the RHS as

$$\left.\begin{array}{lcl}
Ro &=& \theta/2 \\
U_d &=& \theta/2 \\
U_s &=& 0 \\
F &=& 8/\theta \\
r &=& \left[4/\left(\gamma_v^3 Ta\right)\right]^{1/4}\ 2/\theta
\end{array}\right\} \qquad \text{(B.1)}$$

Furthermore, the thickness of the $E^{1/3}$-Stewartson layer can be described through the vertical aspect ratio of the annulus and the Taylor number as

$$\delta = \gamma_v^{-1/2} Ta^{-1/6}. \tag{B.2}$$

Using the correspondences, thermal annulus conditions can be converted to those of the minimal baroclinic two-layer model analysed by *Lovegrove et al.* [49] as

$$\left.\begin{array}{rcl} k_1 &=& 2m\pi/\gamma_h \\ K_2 &=& k_1^2 + \pi^2 \\ \Delta_s &=& r\left(1 + r\,Ro\,K^2\right) \\ \Delta_d &=& r\,K^2/\left(K^2+2F\right) + r^2\,Ro\,K^2 \\ \Delta_b &=& r\,\pi^2/\left(\pi^2+2F\right) + r^2\,Ro\,\pi^2 \\ \beta_s &=& \left(\beta/K^2 - U_s\right)\,k_1 \\ \beta_d &=& \left(\beta/\left(K^2+2F\right) - U_s\right)\,k_1 \\ v_s &=& U_d\,k_1 \\ v_d &=& U_d\,\left(K^2-2F\right)/\left(K_1^2+2F\right)\,k_1 \\ \gamma_s &=& 16k_1^3/(16K^2) \\ \gamma_d &=& 16k_1\,\left(k_1^2-2F\right)/\left(6\left(K^2+2F\right)\right) \\ \gamma_b &=& 32F\,k_1/\left(3\left(\pi^2+2F\right)\right) \end{array}\right\} \tag{B.3}$$

The model by *Lovegrove et al.* [49] consists of four equations for the baroclinic wave of zonal and radial mode numbers m and $n = 1$, respectively, in terms of the cosine component C and sine componen, S, for the barotropic and baroclinic vertical modes using subscript s for 'sum' or barotropic and d for 'difference' or baroclinic, as well as an equation for a single mean-flow correction term, A. The coupling between the standard model by *Lovegrove et al.* [49] and the boundary layer adds an equation for the temperature at the interface between the interior and the Stewartson layer, θ in the form of

$$\dot{C}_s = -\Delta_s C_s + \beta_s S_s - (v_s + \gamma_s A)\,S_d \tag{B.4}$$

$$\dot{S}_s = -\beta_s C_s - \Delta_s S_s + (v_s + \gamma_s A)\,C_d \tag{B.5}$$

$$\dot{C}_d = -(v_s + \gamma_d A)\,S_s - \Delta_d C_d + \beta_d S_d \tag{B.6}$$

$$\dot{S}_d = (v_s + \gamma_d A)\,C_s - \beta_d C_d - \Delta_d S_d \tag{B.7}$$

$$\dot{A} = \gamma_b S_d C_s - \gamma_b C_d S_s - \Delta_b A \tag{B.8}$$

$$\dot{\theta} = -\frac{\Delta_b}{\delta} A - \left(\frac{\Delta_b}{\delta} + \frac{1}{Pr} + v_n \exp\left(-Pr\right)\right)\,\theta + \frac{1}{Pr\,(1+gS)} \tag{B.9}$$

While the effect of the waves on the interface temperature is explicit, the reverse effect is implicit in the fact that the forcing parameter as defined in eq.(B.1) depends on the interface temperature.

[1] Ablowitz, M., and H. Segur, *Solitons and the Inverse Scattering Transform*, SIAM Studies in Applied Mathematics, SIAM, Philadelphia, 1981.

[2] Azouni, A., E. W. Bolton, and F. H. Busse, Experimental study of convection columns in a rotating cylindrical annulus, *Geophys. Astrophys. Fluid Dyn.*, *34*, 301–317, 1986.

[3] Barcilon, V., and J. Pedlosky, A unified linear theory of homogeneous and stratified rotating fluids, *J. Fluid Mech.*, *29*, 609 – 621, 1967.
[4] Benjamin, T. B., and J. E. Feir, The disintegration of wave trains on deep water. part I: Theory, *J. Fluid Mech.*, *27*, 417–430, 1967.
[5] Bretherton, F., Resonant interactions between waves. The case of discrete oscillations, *J. Fluid Mech.*, *20*, 457 – 479, 1964.
[6] Buzyna, G., R. L. Pfeffer, and R. Kung, Transitions to geostrophic turbulence in a rotating differentially heated annulus of fluid, *J. Fluid Mech.*, *145*, 377–403, 1984.
[7] Castrejon-Pita, A. A., and P. L. Read, Baroclinic waves in an air-filled thermally driven rotating annulus, *Phys. Rev. E*, *75*, 026,301, 2007.
[8] Charney, J. G., On a physical base for numerical prediction of large-scale motions in the atmosphere, *J. Meteor.*, *6*, 371–385, 1949.
[9] Charney, J. G., Geostrophic turbulence, *J. Atmos. Sci.*, *28*, 1087 – 1095, 1971.
[10] Christiansen, B., Chaos, quasiperiodicity, and interannual variability: Studies of a stratospheric vacillation model, *J. Atmos. Sci.*, *57*(18), 3161–3173, 2000.
[11] Eady, E., Long waves and cyclone waves, *Tellus*, *1*, 33–52, 1949.
[12] Feliks, Y., M. Ghil, and A. W. Robertson, The atmospheric circulation over the North Atlantic as induced by the SST field, *J. Climate*, *24*(2), 522 – 542, doi:10.1175/2010JCLI3859.1, 2011.
[13] Fjørtoft, R., On changes in the spectral distribution of kinetic energy in two-dimensional, nondivergent flow, *Tellus*, *5*, 225 – 230, 1953.
[14] Flór, J.-B., H. Scolan, and J. Gula, Frontal instabilities and waves in a differentially rotating fluid, *J. Fluid Mech.*, *685*, 532 – 542, 2011.
[15] Fowlis, W. W., and R. L. Pfeffer, Characteristics of amplitude vacillation in a rotating, differentially heated fluid annulus determined by a multi-probe technique, *J. Atmos. Sci.*, *26*, 100–108, 1969.
[16] Früh, W.-G., Low-order models of wave interactions in the transition to baroclinic chaos, *Nonlin. Proc. Geophys.*, *3*, 150–165, 1996.
[17] Früh, W.-G., and P. L. Read, Wave interactions and the transition to chaos of baroclinic waves in a thermally driven rotating annulus, *Phil. Trans. R. Soc. Lond. (A)*, *355*, 101–153, 1997.
[18] Früh, W.-G., and P. L. Read, Experiments in a barotropic rotating shear layer. I: Instability and steady vortices, *J. Fluid Mech.*, *383*, 143–173, 1999.
[19] Früh, W.-G., P. Maubert, P. Read, and A. Randriamampianina, DNS of structural vacillation in the transition to geostrophic turbulence, in *Advances in Turbulence XI*, edited by J.M.L.M. Palma and A. Silva Lopes, no. 117 in Springer Proceedings in Physics, pp. 432–434, Springer Verlag, Porto, 2007.
[20] Guckenheimer, J., and G. Buzyna, Dimension measurements for geostrophic turbulence, *Phys. Rev. Lett.*, *51*, 1438–1441, 1983.
[21] Harlander, U., T. von Larcher, Y. Wang, and C. Egbers, PIV- and LDV-measurements of baroclinic wave interactions in a thermally driven rotating annulus, *Exp. Fluids*, *51*(1), 37–49, 2011.
[22] Hart, J. E., A laboratory study of baroclinic instability, *Geophys. Fluid Dyn.*, *3*, 181–209, 1972.
[23] Hart, J. E., On the behaviour of large amplitude baroclinic waves, *J. Atmos. Sci.*, *30*, 1017–1034, 1973.
[24] Hart, J. E., The modulation of an unstable baroclinic wave field, *J. Atmos. Sci.*, *33*, 1874–1889, 1976.
[25] Hart, J. E., Finite amplitude baroclinic instability, *Ann. Rev. Fluid Mech.*, *11*, 147–172, 1979.
[26] Hart, J. E., Wavenumber selection in nonlinear baroclinic instability, *J. Atmos. Sci.*, *38*, 400–408, 1981.
[27] Hasselmann, K., A criterion for nonlinear wave stability, *J. Fluid Mech.*, *30*, 737 – 739, 1967.
[28] Hide, R., Some experiments on thermal convection in a rotating liquid, *Qr. J. Roy. Met. Soc.*, *79*, 161, 1953.
[29] Hide, R., An experimental study of thermal convection in a rotating liquid, *Phil. Trans. R. Soc. Lond. (A)*, *250*, 441–478, 1958.
[30] Hide, R., Regimes of sloping thermal convection in a rotating liquid annulus, *Geophys. Astrophys. Fluid Dyn.*, *105*(2-3), 117–127, 2011.
[31] Hide, R., and P. J. Mason, Baroclinic waves in a rotating fluid subject to internal heating, *Phil. Trans. R. Soc. Lond. A*, *268*, 201–232, 1970.
[32] Hide, R., and P. J. Mason, Sloping convection in a rotating fluid, *Advances in Physics*, *24*, 47–99, 1975.
[33] Hide, R., P. J. Mason, and R. A. Plumb, Thermal convection in a rotating fluid subject to a horizontal temperature gradient: spatial and temporal characteristics of fully developed baroclinic

waves, *J. Atmos. Sci.*, *34*, 930–950, 1977.
[34] Hignett, P., Characteristics of amplitude vacillation in a differentially heated rotating fluid annulus, *Geophys. Astrophys. Fluid Dyn.*, *31*, 247–281, 1985.
[35] Hignett, P., A. A. White, R. D. Carter, W. D. N. Jackson, and R. M. Small., A comparison of laboratory measurements and numerical simulations of baroclinic wave flows in a rotating cylindrical annulus, *Qr. J. Roy. Met. Soc.*, *111*, 131–154, 1985.
[36] Jacoby, T., P. Read, P. Williams, and R. Young, Generation of inertia-gravity waves in the rotating thermal annulus by a localised boundary layer instability, *Geophys. Astrophys. Fluid Dyn.*, *105*(203), 161–181, doi:10.1080/03091929.2011.560151, 2011.
[37] James, I. N., P. R. Jonas, and L. Farnell, A combined laboratory and numerical study of fully developed steady baroclinic waves in a cylindrical annulus, *Qr. J. Roy. Met. Soc.*, *107*, 51–78, 1981.
[38] Jonas, P. R., Some effects of boundary conditions and fluid properties on vacillation in thermally driven rotating flow in an annulus, *Geophys. Astrophys. Fluid Dyn.*, *18*, 1–23, 1981.
[39] Klein, P., Transitions to chaos in unstable baroclinic systems: a review, *Fluid Dyn. Res.*, *5*, 235–254, 1990.
[40] Koo, S., A. Robertson, and M. Ghil, Multiple regimes and low-frequency oscillations in the Southern Hemisphere's zonal-mean flow, *J. Geophys. Res. - Atmospheres*, *107*(D21), doi: 10.1029/2001JD001353, 2002.
[41] Lappa, M., *Rotating Thermal Flows in Natural and Industrial Processes*, John Wiley & Sons, 2012.
[42] Lewis, G., Effects of Prandtl number on the axisymmetric to nonaxisymmetric transition in the differentially heated rotating annulus, in *Modelling Atmospheric and Oceanic Flow: Insights from laboratory experiments and numerical simulations.*, edited by T. von Larcher and P. D. Williams, Americal Geophysical Union, 2013.
[43] Lindborg, E., The energy cascade in a strongly stratified fluid, *J. Fluid Mech.*, *550*, 207–242, 2006.
[44] Lindzen, R., R. Farrell, and D. Jacqmin, Vacillations due to wave interference — applications to the atmosphere and to annulus experiments, *J. Atmos. Sci.*, *39*, 14–23, 1982.
[45] Lorenz, E. N., Available potential energy and the maintenance of the general circulation, *Tellus*, *7*, 157–167, 1955.
[46] Lorenz, E. N., Deterministic nonperiodic flow, *J. Atmos. Sci.*, *20*, 130–141, 1963.
[47] Lorenz, E. N., The mechanics of vacillation, *J. Atmos. Sci.*, *20*, 448–464, 1963.
[48] Lovegrove, A., I. Moroz, and P. Read, Bifurcations and instabilities in rotating two-layer fluids:I. f-plane, *Nonlin. Proc. Geophys.*, *8*, 21 – 36, 2001.
[49] Lovegrove, A., I. Moroz, and P. Read, Bifurcations and instabilities in rotating two-layer fluids:II. β-plane, *Nonlin. Proc. Geophys.*, *9*, 280 – 309, 2002.
[50] Lu, H., and T. L. Miller, Characteristics of annulus baroclinic flow structure during amplitude vacillation, *Dyn. Atmos. Oceans*, *27*, 485–503, 1997.
[51] Lu, H. I., T. L. Miller, and K. A. Butler, A numerical study of wave-number selection in the baroclinic annulus flow system, *Geophys. Astrophys. Fluid Dyn.*, *75*(1), 1–19, 1994.
[52] Maubert, P., and A. Randriamampianina, Transition vers la turbulence géostrophique pour un écoulement d'air en cavité tournante différentiellement chauffée, *C. R. Méchanique*, *330*, 365–370, 2002.
[53] McEwan, A., D. Mander, and R. Smith, Forced resonant second-order interaction between damped internal waves, *J. Fluid Mech.*, *55*, 589 – 608, 1972.
[54] Nastrom, G. D., and K. S. Gage, A climatology of atmospheric wavenumber spectra observed by commercial aircraft, *J. Atmos. Sci.*, *42*(950 - 960), 1985.
[55] Ohlsen, D. R., and J. E. Hart, Nonlinear interference vacillation, *Geophys. Astrophys. Fluid Dyn.*, *45*, 213–235, 1989.
[56] Or, A. C., and F. H. Busse, Convection in a rotating cylindrical annulus: Part 2. Transitions to asymmetric and vacillating flow, *J. Fluid Mech.*, *174*, 313–326, 1987.
[57] Pedlosky, J., The nonlinear dynamics of baroclinic wave ensembles, *J. Fluid Mech.*, *102*, 169–209, 1981.
[58] Pedlosky, J., *Geophysical Fluid Dynamics*, second ed., Springer-Verlag, Berlin, Heidelberg, New York, 1987.
[59] Pedlosky, J., and C. Frenzen, Chaotic and periodic behaviour of finite-amplitude baroclinic waves, *J. Atmos. Sci.*, *37*, 1177–1196, 1980.
[60] Pfeffer, R. L., and Y. Chiang, Two kinds of vacillation in rotating laboratory experiments., *Monthly Weather Review*, *95*, 75 – 82, 1967.
[61] Pfeffer, R. L., G. Buzyna, and W. W. Fowlis, Synoptic features and energetics of wave-amplitude

vacillation in a rotating, differentially-heated fluid, *J. Atmos. Sci.*, *31*, 622–645, 1973.
[62] Pfeffer, R. L., G. Buzyna, and R. Kung, Time-dependent modes of thermally driven rotating fluids, *J. Atmos. Sci.*, *37*, 2129–2149, 1980.
[63] Pfeffer, R. L., G. Buzyna, and R. Kung, Relationships among eddy fluxes of heat, eddy temperature variances and basic-state temperature parameters in thermally driven rotating fluids, *J. Atmos. Sci.*, *37*, 2577–2599, 1980.
[64] Pfeffer, R. L., S. Applequist, R. Kung, C. Long, and G. Buzyna, Progress in characterizing the route to geostrophic turbulence and redesigning thermally driven rotating annulus experiments, *Theor. Comput. Fluid Dyn.*, *9*, 253–267, 1997.
[65] Phillips, N. A., A simple three-dimensional model for the study of large-scale extratropical flow patterns, *J. Meteor.*, *8*, 381–394, 1951.
[66] Plumb, R. A., The stability of small amplitude Rossby waves in a channel, *J. Fluid Mech.*, *80*, 705–720, 1977.
[67] Pogoreltsev, A., A. Kanukhina, E. Suvorova, and E. Savenkova, Variability of planetary waves as a signature of possible climatic changes, *Journal of Atmospheric and Solar-Terrestrial Physics*, *71*(14 - 15), 1529 – 1539, doi:10.1016/j.jastp.2009.05.011, 2009.
[68] Randriamampianina, A., and E. Crespo Del Arco, High resolution method for direct numerical simulation of the instability and transition in a baroclnic cavity, in *Modelling Atmospheric and Oceanic Flow: Insights from laboratory experiments and numerical simulations.*, edited by T. von Larcher and P. D. Williams, Wiley, 2014.
[69] Randriamampianina, A., W.-G. Früh, P. L. Read, and P. Maubert, Direct numerical simulations of bifurcations in an air-filled rotating baroclinic annulus, *J. Fluid Mech.*, *561*, 359–389, 2006.
[70] Read, P., A combined laboratory and numerical study of heat transport by baroclinic eddies and asixymmetric flows, *J. Fluid Mech.*, *489*, 301 – 323, doi:10.1017/S002211200300524X, 2003.
[71] Read, P. L., M. J. Bell, D. W. Johnson, and R. M. Small, Quasi-periodic and chaotic flow regimes in a thermally-driven, rotating fluid annulus, *J. Fluid Mech.*, *238*, 599–632, 1992.
[72] Read, P. L., P. Maubert, A. Randriamampianina, and W.-G. Früh, Direct numerical simulation of transitions towards structural vacillation in an air-filled, rotating, baroclinic annulus, *Phys. Fluids*, *20*(044107), 1–17, 2008.
[73] Schnaubelt, M., and F. H. Busse, Convection in a rotating cylindrical annulus: Part 3. Vacillating and spatially modulated flows, *J. Fluid Mech.*, *245*, 155–173, 1992.
[74] Sitte, B., and C. Egbers, Higher order dynamics of baroclinic waves, in *Physics of Rotating Fluids*, edited by C. Egbers and G. Pfister, pp. 355–375, Springer Verlag, Berlin Heidelberg New York, 2000.
[75] Smith, R. K., On limit cycles and vacillating baroclinic waves, *J. Atmos. Sci.*, *31*, 2008–2011, 1974.
[76] Son, S., and S. Lee, Preferred modes of variability and their relationship with climate change, *J. Climate*, *19*(10), 2063–2075, doi:10.1175/JCLI3705.1, 2006.
[77] Studer, S., K. Hocke, and N. Kämpfer, Intraseasonal oscillations of stratospheric ozone above switzerland, *J. Atmos. Solar-Terrestrial Phys.*, *74*, 180 – 198, doi:10.1016/j.jastp.2011.10.020, 2012.
[78] Tamaki, K., and K. Ukaji, Radial heat transport and azimuthally averaged temperature fields in a differentially heated rotating fluid annulus indergoing amplitude vacillation, *J. Met. Soc. Japan*, *63*, 168, 1985.
[79] Tamaki, K., and K. Ukaji, Characteristics of tilted-trough vacillation in a differentially heated rotating fluid annulus, *J. Met. Soc. Japan*, *71*, 553–566, 1993.
[80] von Larcher, T., and C. Egbers, Experiments on transitions of baroclinic waves in a differentially heated rotating annulus, *Nonlin. Proc. Geophys.*, *12*(6), 1033–1041, 2005.
[81] Waite, M., and P. Bartello, The transition from geostrophic to stratified turbulence, *J. Fluid Mech.*, *568*, 89–108, 2006.
[82] Watterson, I., Zonal wind vacillation and its interaction with the ocean: Implications for interannual variability and predictability, *J. Geophys. Res. - Atmospheres*, *106*(D20), 23,965 – 23,975, doi: 10.1029/2000JD000221, 2001.
[83] Weng, H.-Y., and A. Barcilon, Wave structure and evolution in baroclinic flow regimes, *Quart.J.R.Met.Soc.*, *113*, 1271–1294, 1987.
[84] Weng, H.-Y., and A. Barcilon, Wavenumber transition and wavenumber vacillation in Eady-type baroclinic flows, *Quart.J.R.Met.Soc.*, *114*, 1253–1269, 1988.
[85] Weng, H.-Y., A. Barcilon, and J. Magnan, Transitions between baroclinic flow regimes, *J. Atmos. Sci.*, *43*, 1760–1777, 1986.
[86] White, H., and E. Koschmieder, Convection in a rotating, laterally heated annulus. Pattern velocities and amplitude oscillations, *Geophys. Astrophys. Fluid Dyn.*, *18*, 301–320, 1981.

[87] Young, R. M. B., and P. L. Read, Flow transitions resembling bifurcations of the logistic map in simulations of the baroclinic rotating annulus, *Physica D - Nonlinear Phenomena*, doi: 10.1016/j.physd.2008.02.014, 2008.

[88] Zakharov, V., Stability of periodic waves of finite amplitude on the surface of a deep fluid, *J. Appl. Mech. Tech. Phys.*, *9*, 190 – 194, 1968.